



Contents lists available at ScienceDirect

International Journal of Solids and Structures

journal homepage: www.elsevier.com/locate/ijsolstr

Internal loops in superelastic shape memory alloy wires under torsion – Experiments and simulations/predictions

Ashwin Rao^a, Annie Ruimi^b, Arun R. Srinivasa^{a,b,*}^a Department of Mechanical Engineering, Texas A&M University, College Station, TX 77843-3123, United States^b Department of Mechanical Engineering, Texas A&M University at Qatar, Doha, Qatar

ARTICLE INFO

Article history:

Received 22 March 2014

Received in revised form 30 August 2014

Available online xxxxx

Keywords:

Shape memory alloy (SMA)

Superelastic effect

Internal loops

Torsion

Design

Return point memory (RPM)

Hysteresis

Preisach

Thermomechanical

ABSTRACT

Understanding torsional responses of shape memory alloy (SMA) specimens under partial or fully transformed cases with internal loops is of particular importance as the entire response might not be always utilized and only a portion of the entire response (internal loop) might be of significance to designers. In this work, we present experimental results of large complex loading and unloading torsional cycles which were conducted on superelastic SMA wires, under isothermal conditions with the purpose of elucidating the torsional internal loop response during loading and unloading. Such data hereto has not been available in open literature. Utilizing this data, we model the torsional response of superelastic SMA wires subjected to various loading and unloading situations that can result in different extents of transformation.

A thermodynamically consistent Preisach model (Rao and Srinivasa, 2013) captures such complex internal loops with a high degree of precision by modeling driving force for phase transformation vs. volume fraction of martensite relationships. This approach is different from capturing purely phenomenological stress–strain or stress–temperature Preisach models. The thermodynamic approach utilized here has broader predictive capability. The model predictions indicate good agreement with the internal loop structures even though only the outer loop information was used for model calibration. The addition of a single inner loop information for model calibration greatly improves the predictions.

© 2014 Elsevier Ltd. All rights reserved.

1. Introduction

Shape memory alloy (SMA) components like wires, tubes and springs under torsion are being used in many applications due to their ability to recover large strokes and deliver near constant forces over large displacements (Ghosh et al., 2013; NDC; Rao and Srinivasa, 2013, 2014). During service, such components can be subjected to load reversals before complete transformation is achieved which may result in partial or complex hysteretic internal loops¹ either during the loading or unloading stage of the response (Khandelwal and Buravalla, 2011; Miyazaki and Otsuka, 1989).

* Corresponding author at: 3123, Mechanical Engineering Office Building, Texas A&M University, College Station, TX 77843-3123, United States. Tel.: +1 979 862 3999; fax: +1 979 845 3081.

E-mail address: asrinivasa@tamu.edu (A.R. Srinivasa).

¹ An internal loop is a consequence of intermediate loading and unloading preceding complete transformation that results in smaller hysteretic responses which closely mimics the characteristics of outer loops that is fully transformed. The area of these smaller hysteretic loops depends on the extent of the loading and unloading level which the component is subjected to during service within the transformation regime (plateau region) (Khandelwal and Buravalla, 2011; Miyazaki and Otsuka, 1989).

Capturing such internal loop responses is important from an application standpoint because in many cases, knowledge of the entire response proves to be unnecessary and only a partial internal loop might be of significance to designers or application developers (Bogue, 2009; Machado and Savi, 2003). For example, in civil engineering applications, SMA components are being used as seismic resisting systems due to their excellent energy dissipation and re-centering capabilities during which they can be subjected to repeated loading and unloading cycles at different loading rates and amplitudes (Song et al., 2006; Speicher et al., 2009; Saadat et al., 2002; DesRoches and Smith, 2004; Wilson and Wesolowsky, 2005; Williams et al., 2002; Rao and Srinivasa, 2013). Such repeated loading and unloading cycles may result in smaller hysteretic inner loops. For orthodontic applications, SMA wires and springs are employed to deliver constant forces over large strokes for space closure and tooth movement (Drake et al., 1982; Miura et al., 1986, 1988; Rao and Srinivasa, 2013). In some other biomedical applications, SMA components are employed for a certain part of the plateau regions over the transformation region and unloaded later resulting in partially transformed loops (Kapila and Sachdeva, 1989; Manhartsberger and Seidenbusch, 1996; El Feninat et al., 2002; Spinella et al., 2010).

Understanding the response of SMA springs and wires subjected to torsional loading has been of significant interest among researchers (Saadat et al., 2002; Drake et al., 1982). As these SMA components twist under torsion, the phase transformation front propagates from outer fibers inwards to the core of the cross-section and its location is not known a priori (Tobushi and Tanaka, 1991; Rao and Srinivasa, 2013). In addition, because the shear strain is quite negligible at the core, a fully transformed case is only possible at high degrees of twist (Rao and Srinivasa, 2013; Mirzaeifar et al., 2011; Mirzaeifar et al., 2010). In partially transformed cases, one can expect the presence of an untransformed austenitic core due to small shear strains at the core (Rao and Srinivasa, 2013). It is thus important for designers to study such partially transformed cases and internal loops to predict SMA component responses under different extent of loading and unloading levels more accurately.

Torsional tests on SMA springs, wires/rods have been reported in the literature. Aguiar et al. (2010), Attanasi et al. (2011), Barwart (1996), Mirzaeifar et al. (2011), Miura et al. (1986, 1988) and Rao and Srinivasa (2013) have reported force – stroke relationships for SMA springs. Clearly, the springs were partially transformed in all the reported cases as there were no distinct upper and lower plateaus or elastic deformation of stress induced martensite (SIM) as observed under fully transformed cases (similar to tension load cases). However, data of fully transformed springs is scanty due to difficulty in testing compression/extension helical springs over large strokes.

On the other hand, only a few studies on understanding torque–twist relationships for SMA wires under pure torsion are available in the literature. Doaré et al. (2012) performed experiments on superelastic SMA wires under different angles of twists (see experimental results – Fig. 4 in Doaré et al., 2012) with the maximum twist in their tests being limited to 450° twist. However, from these test results it is unclear if a fully martensitic wire is obtained at higher twists as there was no elastic deformation of SIM observed in these experiments. Chapman et al. (2011) in their work studied the response of three superelastic wires with different diameters under torsion until failure and their results clearly illustrates that one can observe a fully transformed wire response (similar to pure tension responses) under higher degrees of twist (see Figs. 2 and 3 in Chapman et al., 2011). Prahlad and Chopra (2007) and Dolce and Cardone (2001a,b) have attempted to study torque–twist behavior of SMA rods under pure torsion for partially transformed cases. Some combined loading cases (tension–torsion) on SMA components like rods and tubes have also been reported in literature (Andani et al., 2013a; Grabe and Bruhns, 2008; Han et al., 2005; Lim and McDowell, 1999; McNaney et al., 2003; Sun and Li, 2002).

In all the available literature on the topic, simple torsional loading and unloading cases at different extent of twists is discussed. Understanding internal loop responses have been limited to tension loading cases (see Fig. 4 in Huo and Müller, 1993, Figs. 2, 4a and b in LExcellent and Tobushi, 1995, Figs. 3–12 in Tanaka et al., 1994, Fig. 3 in Sittner et al., 1995, Fig. 6 in Liu et al., 1998, Figs. 3 and 4 in Sittner et al., 2000, Fig. 12 in Müller and Seelecke, 2001, Fig. 6 in Dolce and Cardone, 2001a, Fig. 3 in Ortun and Delaey, 2002, Fig. 3 in Matsuzaki et al., 2002, Figs. 4 and 7 in DesRoches et al., 2003, Fig. 5 in Ikeda et al., 2004, Figs. 1–4 in Savi and Paiva, 2005, Fig. 2–4 in Kumar et al., 2007, Fig. 6 in Heintze and Seelecke, 2008, Fig. 7 in Müller, 2012, etc. for some illustrations under tension loading case). The study of internal loops (under loading and unloading stages) in wires under torsional loading is not addressed.

In this paper, an effort to investigate the response of superelastic SMA wires subjected to torsional loading and unloading cases with internal loops is undertaken. The main emphasis here is on

experiments and modeling of internal loops. An Instron micro-torsion apparatus is used to conduct various test cases. The shape of inner loops compared to outer/major loops is examined and the return point memory (RPM) or sink point memory (SPM) aspects in the torsional response is investigated (see Fig. 8 in Khandelwal and Buravalla, 2011 for an illustration under tension loading). RPM and SPM provides important information on the ability of SMA components to return back to its original unloading point upon completion of a smaller hysteretic loop and is of particular importance to designers. SMA components showing good RPM/SPM characteristics is a desirable feature that indicates minimal residual/irreversible deformations after repeated complete or partial transformations.

In the second part of the paper, following Rao and Srinivasa (2013), a thermodynamically consistent Preisach model is used to predict the response of twisted wires. The key idea in this model is the decomposition of the entire hysteretic response into a thermoelastic and a dissipative part using a two species Gibbs potential (Doraiswamy, 2010; Doraiswamy et al., 2011; Rao and Srinivasa, 2013, 2014; Rao, 2013). Quantities measured experimentally such as torque and angle of twist serve as input parameters to the model. By doing so and rather than solving for non-homogeneous shear stresses across the specimen cross-sections (Rao and Srinivasa, 2013; Rao, 2013), direct torque–twist relationships at the component level are modeled.² Models capable of predicting responses directly in terms of torque angle of twist would play a vital role in designing many SMA devices across engineering disciplines from both structural and control systems standpoint (Rao and Srinivasa, 2013, 2014; Rao, 2013).

Such a modeling approach also offers the advantage of being able to easily capture complex hysteretic responses with multiple internal loops both under load or displacement controlled experiments (Doraiswamy, 2010; Doraiswamy et al., 2011; Rao and Srinivasa, 2013, 2014; Rao, 2013). An interesting feature of the thermodynamic Preisach model is that it has some predictive capability and is not merely interpolative. Even for complex loading and unloading paths, one can predict the inner loop behavior with reasonable accuracy by using the outer loop data alone with no additional requirements. This means that a single loading/unloading cycle is all that is required to calibrate the model and can be used to simulate other complex loading-unloading paths with sufficient fidelity, a useful feature from a designer point of view.

The paper is organized as follows: in Sections 2 and 3, details on the material, apparatus and experimental protocols are presented. Various partially transformed cases obtained under different loading and unloading scenarios are discussed in Section 4. In Section 5, a two species Gibbs potential is formulated to obtain relationships between the thermodynamic driving force and the volume fraction of martensite using an additive decomposition. Section 6 discusses the details of implementing a discrete Preisach model to capture the driving force-volume fraction of martensite relationship which represent the purely dissipative part of the response. In Section 7,

² The common modeling approach in torsion literature is to replace normal stresses/strains/elastic moduli in 1D constitutive models by its shear counterparts namely shear stresses/strain/shear moduli (Aguiar et al., 2010; Paiva et al., 2005; Savi and Paiva, 2005; Rao and Srinivasa, 2013) or to reduce general 3D constitutive relationships to special 1D pure shear case and use a von Mises equivalent stress approach due to lack of full 3D experimental data (Mirzaeifar et al., 2011, 2010; Chapman et al., 2011). Andani et al. (2013b) and Andani and Elahinia (2014) have also made efforts to compare models of SMA behavior with non-proportional tension–torsion loading paths. Not surprisingly, the use of a simple von Mises equivalent stress approach have been found wanting and other definitions of equivalent stresses and strains have been proposed with resulting improvements in the response. However, the bulk of these cases do not deal with internal loops and partially transformed cases. The model presented in this paper, shares the basic Gibbs potential based formulation of Andani and coworkers but differs in the way in which the martensitic volume fraction evolves.

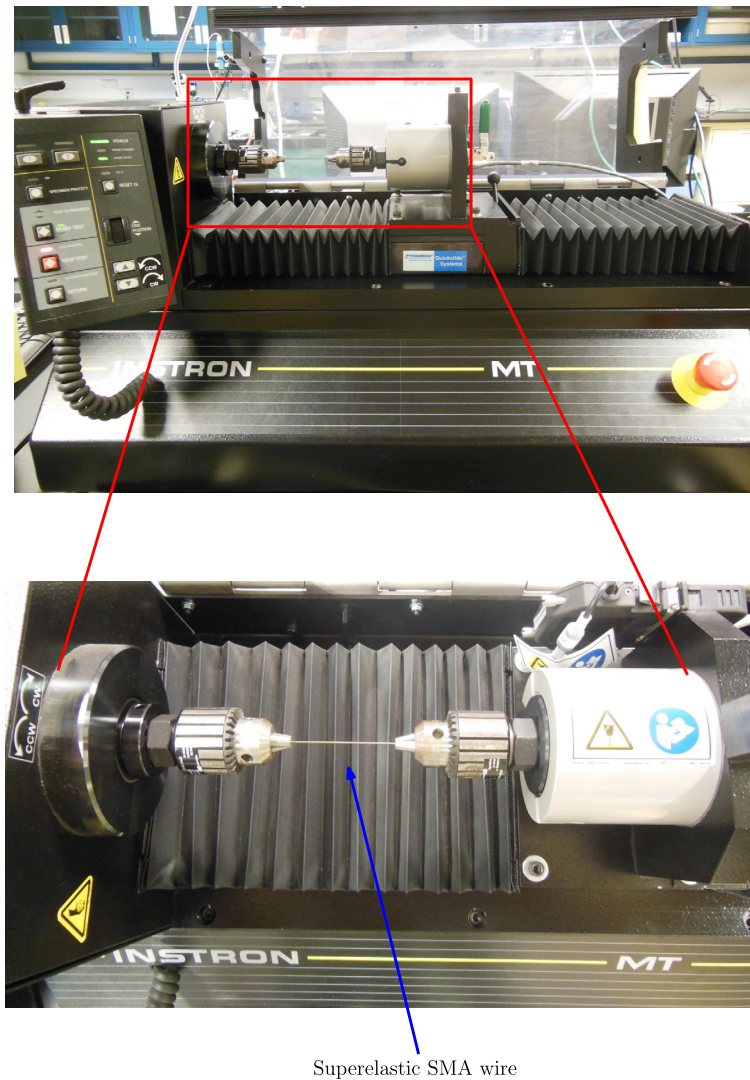


Fig. 1. Experimental set-up showing an Instron® micro-torsion MT series machine with superelastic SMA wire specimens mounted between mechanical collet grips.

prediction of torque vs. angle of twist under load and displacement controlled tests is discussed. Sections 8.1 and 8.2 compares the model predictions with the experimental data. Finally, Section 9 highlights the findings of the work.

2. Material and test apparatus

Superelastic NiTi wires of 0.58 mm diameter were supplied by Small Parts. A series of cyclic twisting–untwisting (loading–unloading) experiments of the wires were conducted at room temperature (298 K) using an Instron® micro-torsion MT series machine available in Texas A&M University at Qatar campus.

Fig. 1 shows the experimental set-up used along with the grip and specimen mounting details. The test setup uses a 2.25 Nm torque cell and a guide rail arrangement for gage length adjustment. With the PARTNER® software supplied by Instron®, torque and twist parameters were continuously monitored as a function of time throughout the test. The software contains a “destructive test option” which allows the user to develop custom designed test protocols by creating various “test zones” that allows programming of customized internal loops (i.e. user defined intermediate loading and unloading levels).

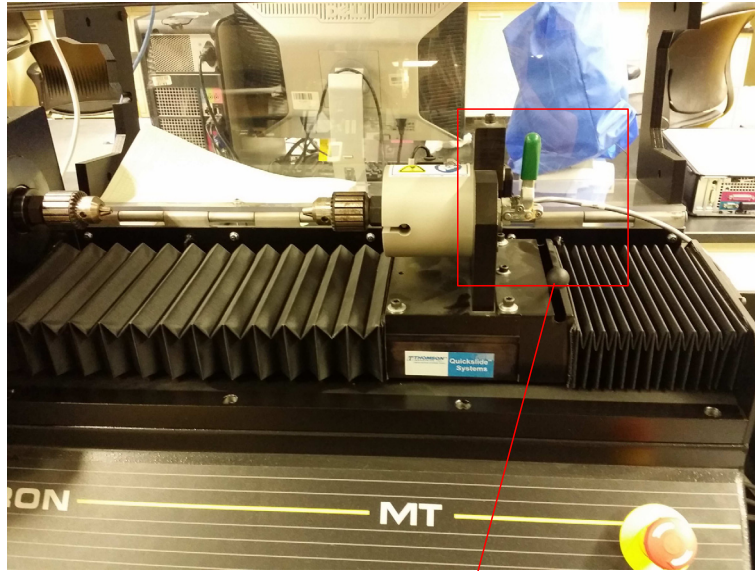
3. Experimental protocols

Wire samples of 60 mm gage length were cut from the as received superelastic SMA wires. The samples were fixed between the mechanical collet grip assemblies³ so as to ensure that there is no axial load on the specimen during the torsion test. A check was made on the frictional resistance of the slider and the frictional loads were verified to be negligible compared to the torsional loads on the wire.⁴

All the tests were twist/displacement controlled with a twisting rate of 2°/s and a maximum twist of 1800°. All the tests were conducted in the clockwise direction and the direction of twisting is insignificant since responses under torsional loading are symmetric in nature (see Figs. 3 and 4 in Doaré et al., 2012 for symmetry illustrations). To ensure repeatability, a minimum of four runs for each test case were conducted (see Fig. 4).

³ The Instron MT-1 microtorsion test rig for wire testing is a specialized machine with a dual linear slide design to provide high torsional stiffness and low axial friction. This machine is specially built to allow both torsional loads without and with specified axial forces (by using dead weights via a pulley arrangement to simulate the effect of axial forces for combined tension-torsion loading experiments). During the torsion test, care was taken to ensure that the cross head was freely sliding as shown in Fig. 2.

⁴ A note on the effect of axial loads along with torsional loading is discussed in Appendix A.



No axial loads were applied for all the test cases discussed here

Fig. 2. The micro-torsion MT series machine is specially built to allow both torsional loads with and without axial forces (by using dead weights via a pulley arrangement to simulate effect of axial loads). During the torsion test, care was taken to ensure that the cross head was freely sliding (i.e. no external axial loads).

4. Experimental runs

4.1. Simple loading and unloading

The procedure to obtain the response of a typical superelastic torsional loading and unloading case consisted of the two steps shown in Fig. 3(a):

- Zone 1 Twist up to 1800° twist (Loading cycle).
- Zone 2 Untwist back to 0° twist (Unloading cycle).

Data recorded for the triangular force function (Fig. 3(a)) is shown in Fig. 3(b) and it clearly shows a non-linear behavior especially during the phase transformation event. The negligible residual deformation upon unloading (torque vs. twist shown in Fig. 3(c)) with well defined plateau stresses⁵ and elastic deformation of SIM is a clear sign of near perfect superelasticity. The torsional response shown in Fig. 3(c) is similar to a classic pseudoelastic tension response of SMA wire.

The test protocol was reapplied on samples subjected to 1500°, 1350°, 900° and 600° maximum twist as shown in Fig. 4(a). The corresponding torque vs. time (Fig. 4(b)) and torque vs. twist (Fig. 4(c)) responses overlap on each other which demonstrate good agreement and test repeatability.

4.2. Multiple internal loops during loading cycle

The procedure to obtain a material response with multiple internal loops (i.e. a case of three internal loops was chosen) during the loading cycle consisted of the following steps: Fig. 5(a)

- Zone 1 Twist up to 600° twist (Loading cycle).
- Zone 2 Untwist back to 300° twist (Unloading cycle).
- Zone 3 Twist up to 900° twist (Loading cycle).
- Zone 4 Untwist back to 600° twist (Unloading cycle).
- Zone 5 Twist up to 1200° twist (Loading cycle).
- Zone 6 Untwist back to 900° twist (Unloading cycle).
- Zone 7 Twist up to 1800° twist (Loading cycle).
- Zone 8 Untwist back to 0° twist (Unloading cycle).

The data recorded for this test run is shown in Fig. 5(b). The torque–twist response Fig. 5(c) exhibits three internal loops (during the loading cycle) and shows almost perfect RPM. The austenitic and martensitic slopes of the internal loops follow the same trend as that of the outer loops.

4.3. Internal loop during loading and unloading cycle

Comparison of an internal loop during loading and unloading cycle was possible using the following protocol shown in Fig. 6(a)

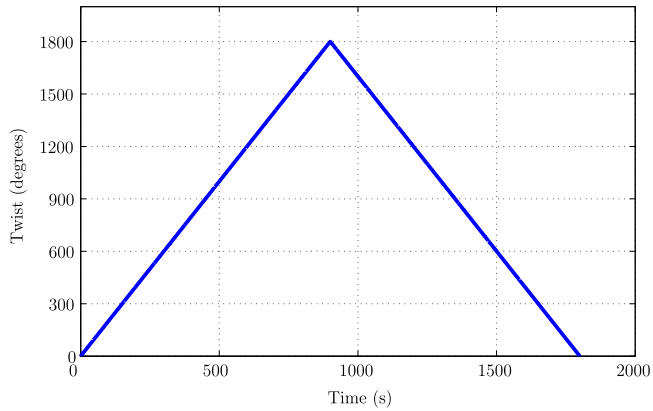
- Zone 1 Twist up to 900° twist (Loading cycle).
- Zone 2 Untwist back to 400° twist (Unloading cycle).
- Zone 3 Twist up to 1800° twist (Loading cycle).
- Zone 4 Untwist back to 800° twist (Unloading cycle).
- Zone 5 Twist up to 1300° twist (Loading cycle).
- Zone 6 Untwist back to 0° twist (Unloading cycle).

Recorded data for this test run with the triangular twist controlled forcing function as input is shown in Fig. 6(b). For the non-linear torque–twist response shown in 6(c), the internal loop during loading and unloading event never intersects the outer loop. In both internal loops, one can observe near perfect RPM with no residual elongation upon complete unloading.

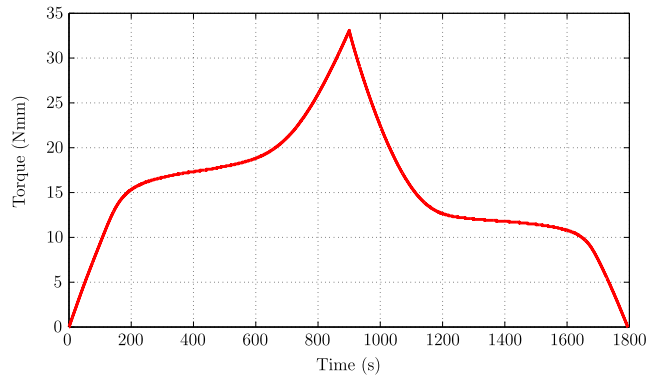
4.4. Complex loading cycle

A complex loading scenario was investigated with the following protocol shown in Fig. 7(a)

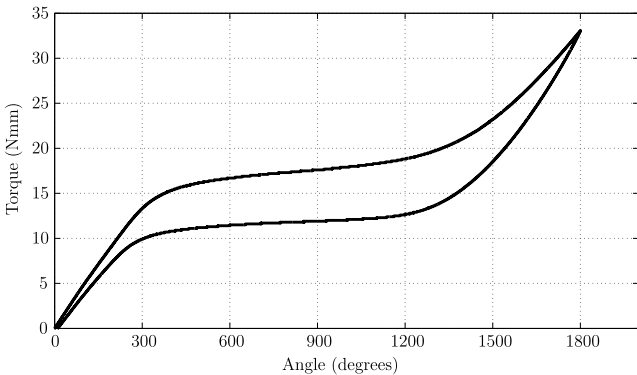
⁵ Plateau stresses are some of the salient features associated with a typical superelastic response under tension loading case as discussed in the ASTM standard F2516-07² (ASTM standard, 2007) for superelastic NiTi materials. The standard defines two plateau stresses – an **Upper plateau strength (UPS)** which is the stress value at 3% strain during loading of the sample and a **Lower plateau strength (LPS)** which is the stress value at 2.5% strain during unloading of sample after has been loaded up to 6% strain.



(a) Twist – time plot



(b) Torque – time plot

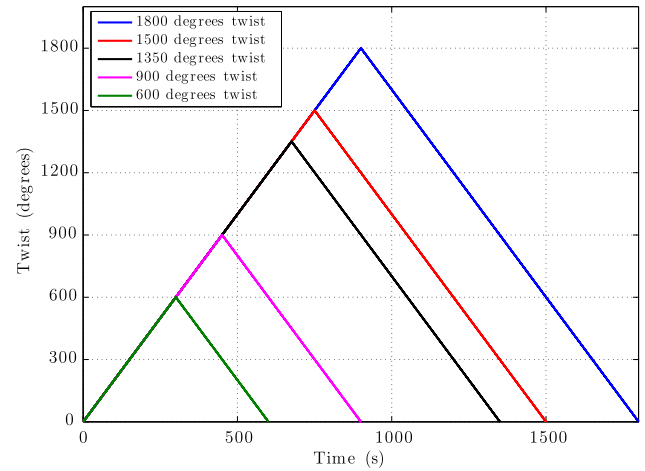


(c) Torque – twist plot

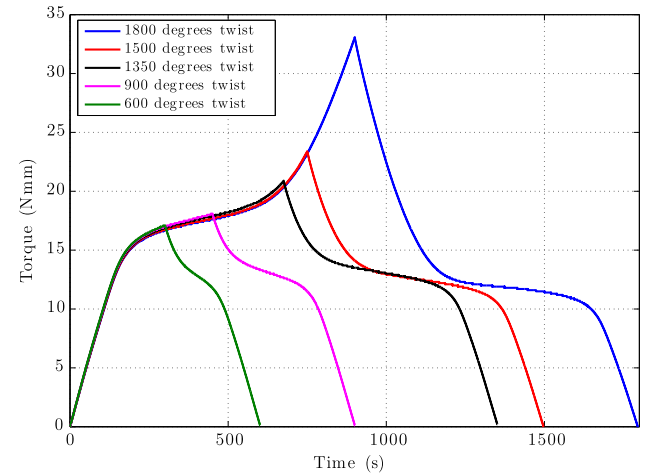
Fig. 3. Figures show the twist-time; torque-time and torque-twist responses for a simple loading and unloading test up to 1800° maximum twist.

- Zone 1 Twist up to 1300° twist (Loading cycle).
- Zone 2 Untwist back to 400° twist (Unloading cycle).
- Zone 3 Twist up to 1100° twist (Loading cycle).
- Zone 4 Untwist back to 600° twist (Unloading cycle).
- Zone 5 Twist up to 900° twist (Loading cycle).
- Zone 6 Untwist back to 800° twist (Unloading cycle).
- Zone 7 Twist up to 1800° twist (Loading cycle).
- Zone 8 Untwist back to 0° twist (Unloading cycle).

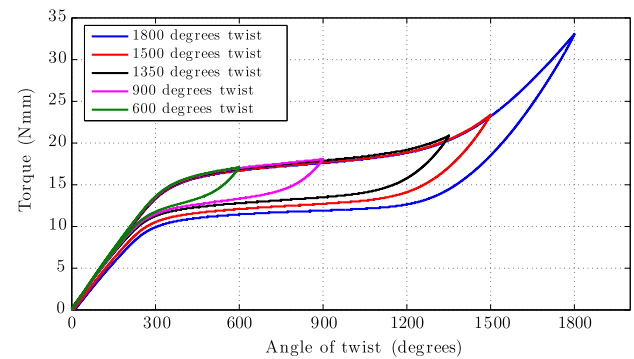
Data recorded for this case is shown in Fig. 7(b). The complex loop response exhibited on the torque-twist plot 7(c) shows that the partially transformed case (internal loops) follows the trend of the fully transformed case (outer loop).



(a) Twist – time plots overlapped for different extents of maximum twists



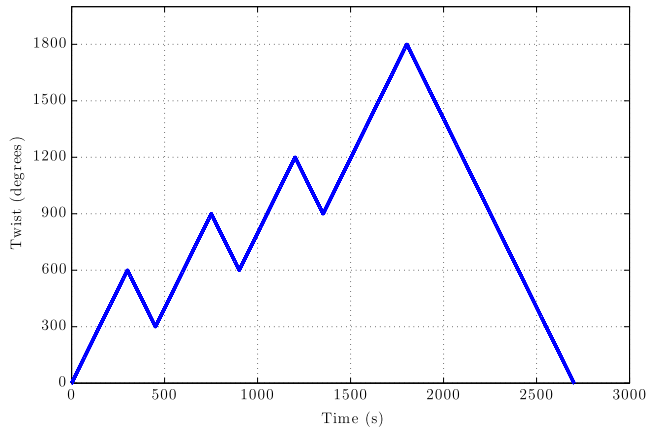
(b) Torque – time plots overlapped for different extents of maximum twists



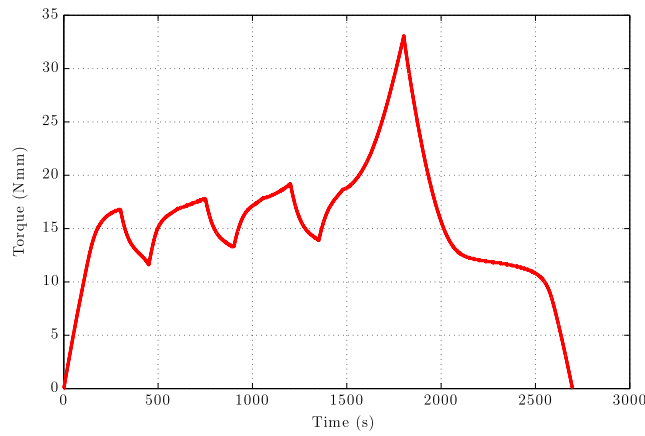
(c) Torque – twist plot

Fig. 4. Figures show the twist-time; torque-time and torque-twist responses for a simple loading and unloading tests with different unloading points of 1500°, 1350°, 900° and 600° maximum twists overlapped on each other and compared against the 1800° twist. All the individual tests were different trials performed on different test specimens which demonstrate good agreement and repeatability.

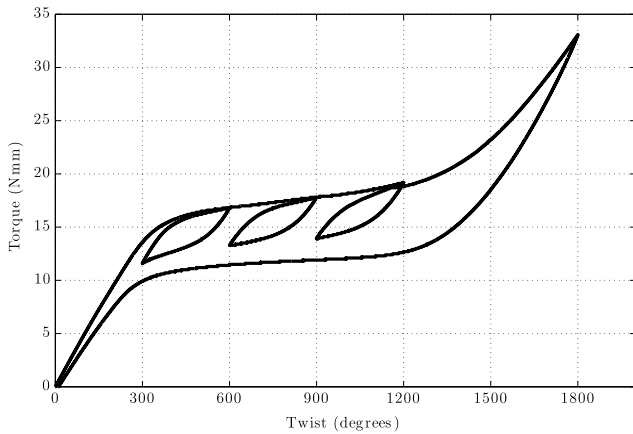
The internal loops never intersect the outer loops regardless of the extent of loading and unloading points selected with the transformation regime (i.e. the plateau stress levels).



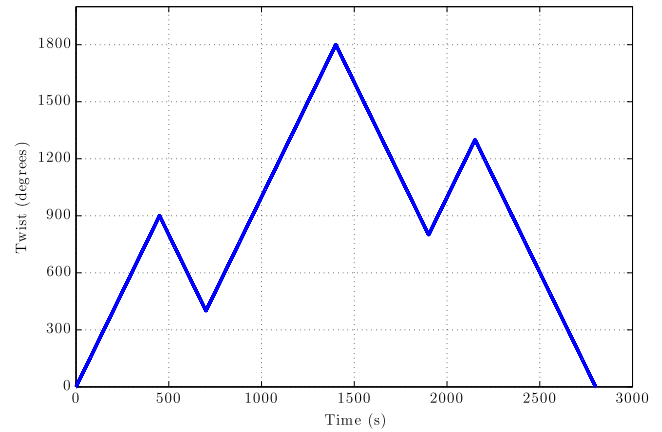
(a) Twist – time plot



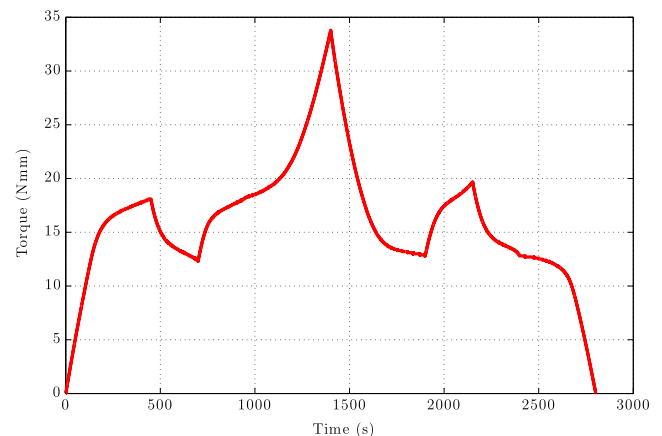
(b) Torque – time plot



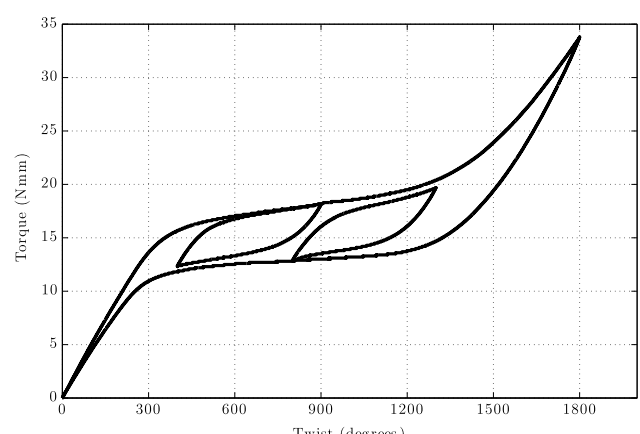
(c) Torque – twist plot



(a) Twist – time plot



(b) Torque – time plot



(c) Torque – twist plot

Fig. 5. Experimental data showing the twist-time; torque-time and torque-twist responses for test up to 1800° maximum twist with three internal loops during the loading cycle.

4.5. Complex loops during unloading cycle

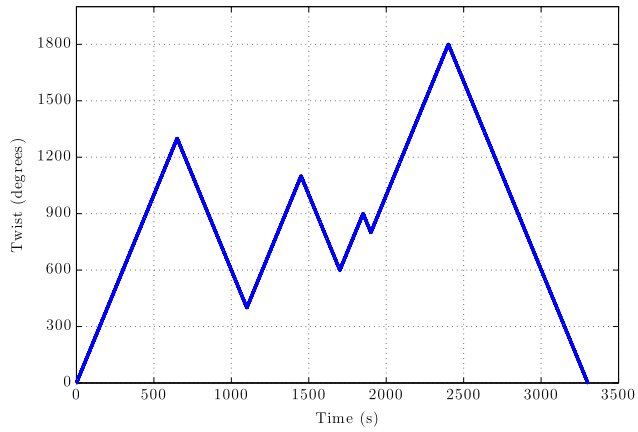
Similar to the previous case, the material behavior for a complex unloading case was recorded using the following protocol shown in Fig. 8(a).

- Zone 1 Twist up to 1800° twist (Loading cycle).
- Zone 2 Untwist back to 400° twist (Unloading cycle).
- Zone 3 Twist up to 1300° twist (Loading cycle).

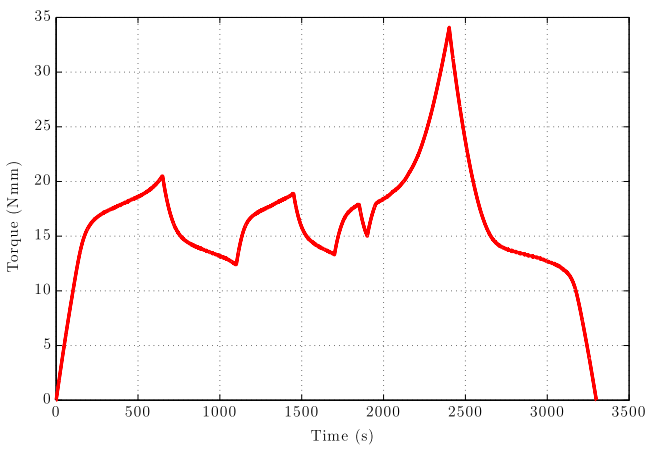
Fig. 6. Figures show the twist-time; torque-time and torque-twist responses for test up to 1800° maximum twist for comparing internal loops during loading and unloading cycle.

- Zone 4 Untwist back to 600° twist (Unloading cycle).
- Zone 5 Twist up to 1100° twist (Loading cycle).
- Zone 6 Untwist back to 800° twist (Unloading cycle).
- Zone 7 Twist up to 900° twist (Loading cycle).
- Zone 8 Untwist back to 0° twist (Unloading cycle).

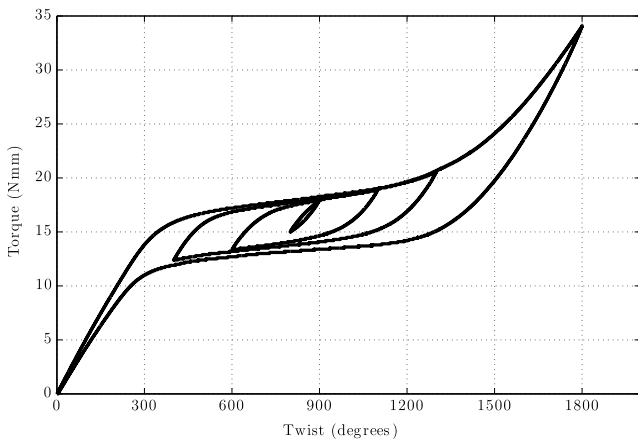
Data recorded for this case is shown in Fig. 8(b). The complete torque-twist response is shown in Fig. 8(c). The complex loops closely mimic the outer loop response but never intersect the outer loop. A good RPM was observed in this case too.



(a) Twist – time plot



(b) Torque – time plot



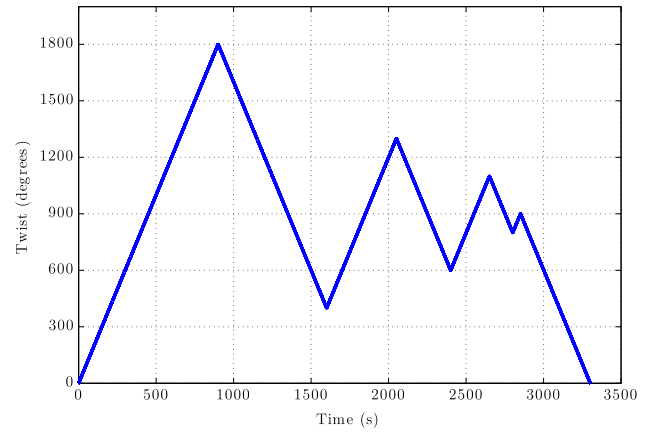
(c) Torque – twist plot

Fig. 7. Figures shows the twist-time; torque-time and torque-twist responses for test up to 1800° maximum twist with a complex internal loops during loading cycle.

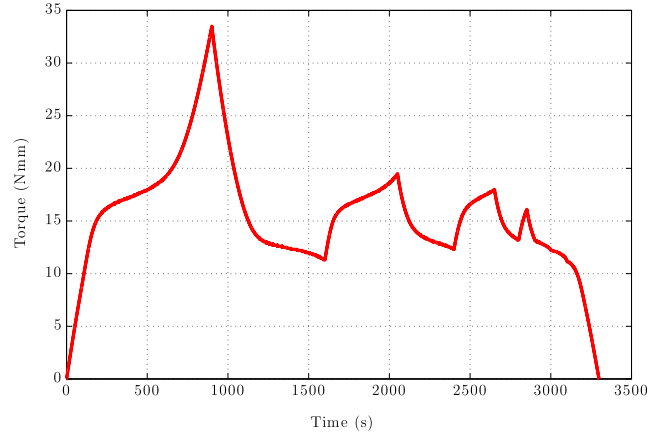
4.6. Complex loading and unloading cycle

A complex unloading cycle with multiple loops was studied with the following protocol as shown in Fig. 9(a)

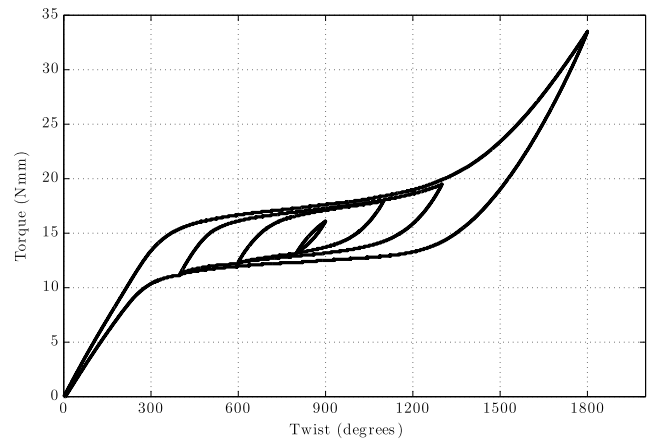
- Zone 1 Twist up to 900° twist (Loading cycle).
- Zone 2 Untwist back to 400° twist (Unloading cycle).
- Zone 3 Twist up to 800° twist (Loading cycle).



(a) Twist – time plot



(b) Torque – time plot



(c) Torque – twist plot

Fig. 8. Figures shows the twist-time; torque-time and torque-twist responses for test up to 1800° maximum twist with a complex internal loops during unloading cycle.

- Zone 4 Untwist back to 500° twist (Unloading cycle).
- Zone 5 Twist up to 700° twist (Loading cycle).
- Zone 6 Untwist back to 600° twist (Unloading cycle).
- Zone 7 Twist up to 1800° twist (Loading cycle).
- Zone 8 Untwist back to 800° twist (Unloading cycle).
- Zone 9 Twist up to 1300° twist (Loading cycle).
- Zone 10 Untwist back to 900° twist (Unloading cycle).
- Zone 11 Twist up to 1200° twist (Loading cycle).

Zone 12 Untwist back to 1000° twist (Unloading cycle).
 Zone 13 Twist up to 1100° twist (Loading cycle).
 Zone 14 Untwist back to 0° twist (Unloading cycle).

Data recorded for this case is shown in Fig. 9(b). The complete torque–twist response is shown in Fig. 9(c). The complex loops under both loading and unloading cases closely mimic the outer loop response but never intersect the outer loop and showing excellent RPM.

5. Model development

As outlined in the introduction, a model capable of simulating complex internal loops is presented here and model predictions are compared against these experimental runs. The model developed by Doraiswamy and his team (Rajagopal and Srinivasa, 1999; Doraiswamy, 2010; Doraiswamy et al., 2011; Rao and Srinivasa, 2013) employs a two species Gibbs potential per unit volume to separate the thermoelastic and the dissipative part of the response. The model⁶ assumes a Gibbs potential function that is a function of torque (T), operating temperature (θ) and the extent of transformation (ξ) i.e. the resulting volume fraction of martensite formed during phase transition.⁷

Consider a SMA wire of diameter d subjected to a torque T about its axis and ϕ denotes the angle of twist per unit length measured during testing.

5.1. Two species Gibbs potential form

The Gibbs potential function is assumed to be comprised of four terms (see Eq. (1)):

1. a linear combination of the strain energy for the two species/phases,
2. an interaction term between the two phases,
3. a term related to the heat capacity difference between the two phases and
4. a term relating to the heat capacity of the austenite.

$$\mathcal{G} = - \left(\frac{\xi T^2}{2G_M J} + \frac{(1-\xi)T^2}{2G_A J} \right) + \overbrace{B\xi(\xi-1)}^2 + \overbrace{(1-\xi)(a+b\theta)}^3 - \overbrace{C\theta(1-\ln\theta)}^4 \quad (1)$$

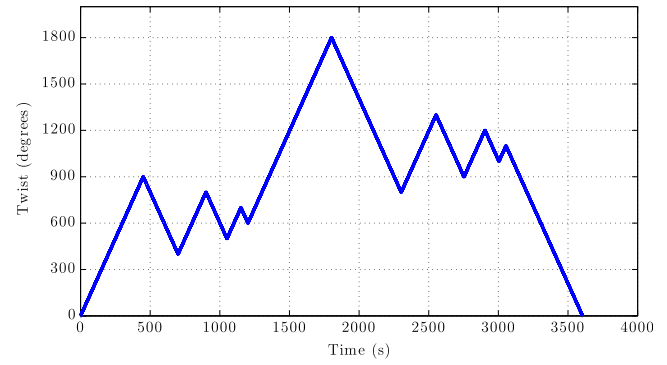
where,

- ξ is the martensite volume fraction; T is the applied torque; G_A and G_M are the austenitic and martensitic shear moduli; $J = \frac{\pi d^4}{32}$ is the polar moment of inertia; B , a and b are constants; θ is the operating temperature and C is the specific heat of austenite

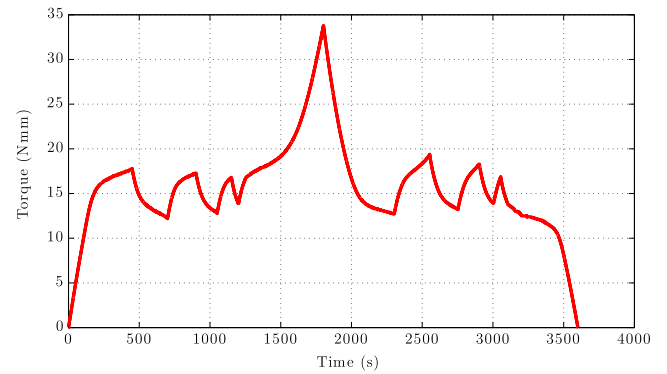
Parameter “ a ” is the internal energy difference between the two phases at 0 K while “ b ” is the entropy difference between the austenite and martensite phases. The constant “ B ” represents the interaction energy between the phases or variants i.e interaction energy between austenite and martensite phases. The two moduli (G_A and G_M) and all the three model constants (a , b and B) can calibrated directly from the experimental torque–twist response.

⁶ The model's capabilities are not restricted to SMA wires and have applications for different SMA components like springs and tubes under torsional loading conditions (see Rao and Srinivasa, 2013; Rao and Srinivasa, 2014 for illustrations).

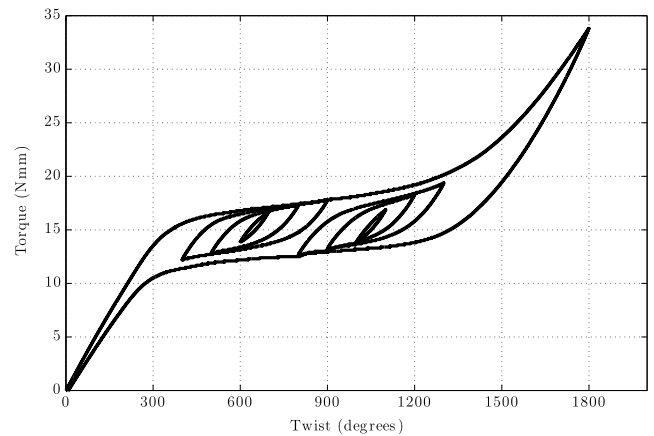
⁷ The two species assumed here are austenite (A) and a single variant of martensite (M). In reality, SMA components could transform from austenite to a combination of many martensite variants (i.e. different variants of un-twinned martensite). For simplicity, it is assumed that all transformation cases are between the two phases A and M for all superelastic responses.



(a) Twist – time plot



(b) Torque – time plot



(c) Torque – twist plot

Fig. 9. Figures shows the twist–time; torque–time and torque–twist responses for test up to 1800° maximum twist with a complex internal loops during both loading and unloading cycles.

Readers are referred to Section 6 from Rao and Srinivasa (2013) for details on parameter identification.

5.2. Macroscopic thermodynamic driving force for phase change

Following Doraiswamy (2010), Doraiswamy et al. (2011) and Rao and Srinivasa (2013), it can be shown that the phase transitions are driven by the thermodynamic driving force which can be obtained from the Gibbs Potential by $\frac{\partial \mathcal{G}}{\partial \xi}$. There are two contributors to the inelastic power. The term $T(\dot{\phi} - \dot{\phi}_e)$ corresponds to a shape change occurring during transformation between two phases. The other term $\left(-\frac{\partial \mathcal{G}}{\partial \xi}\right)$ corresponds to the Gibbs potential

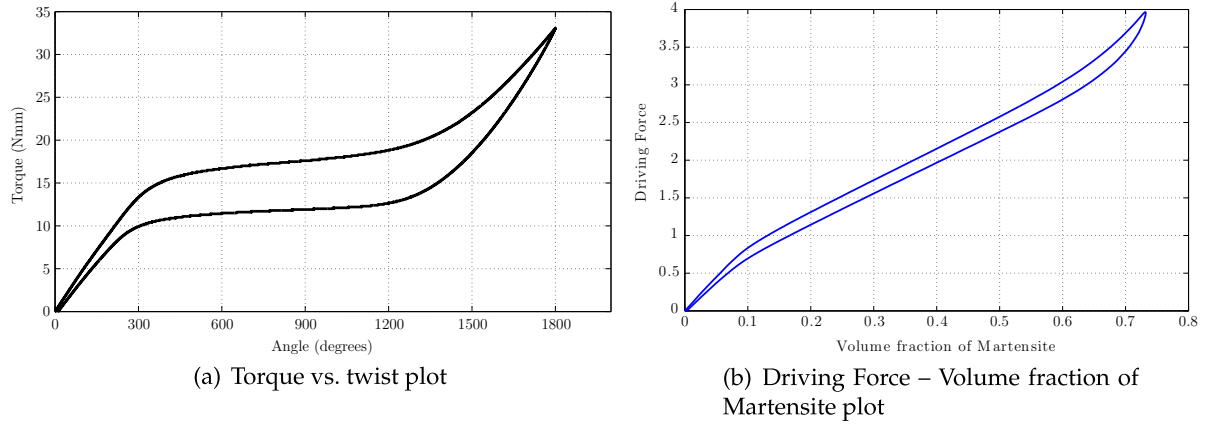


Fig. 10. Torque vs. twist response and corresponding driving force vs. volume fraction of martensite for a simple loading and unloading case of a wire sample twisted up to 1800°.

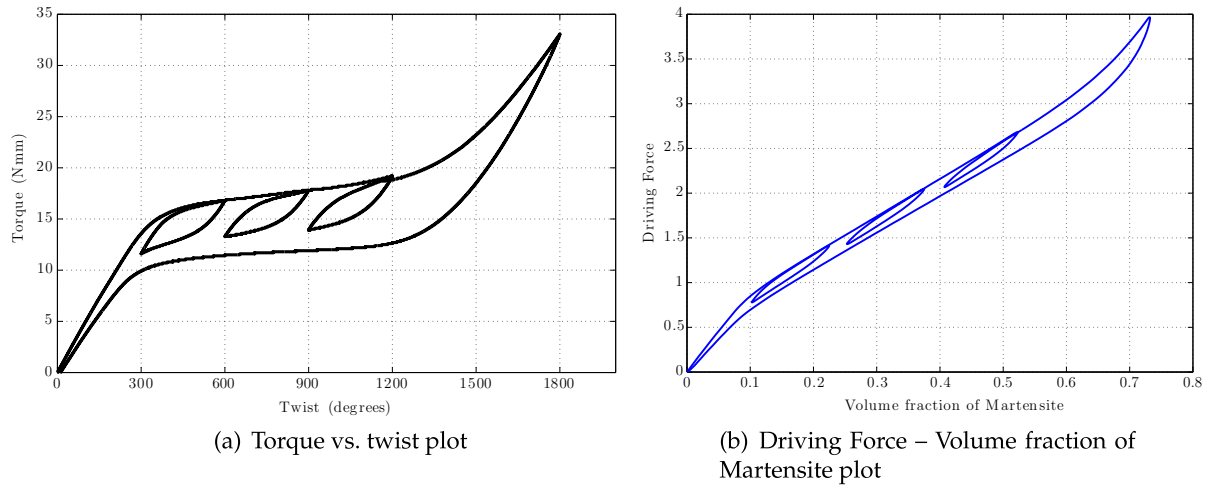


Fig. 11. Torque vs. twist response and its corresponding driving force vs. volume fraction of martensite for wire samples twisted up to 1800° with three internal loops during the loading cycle.

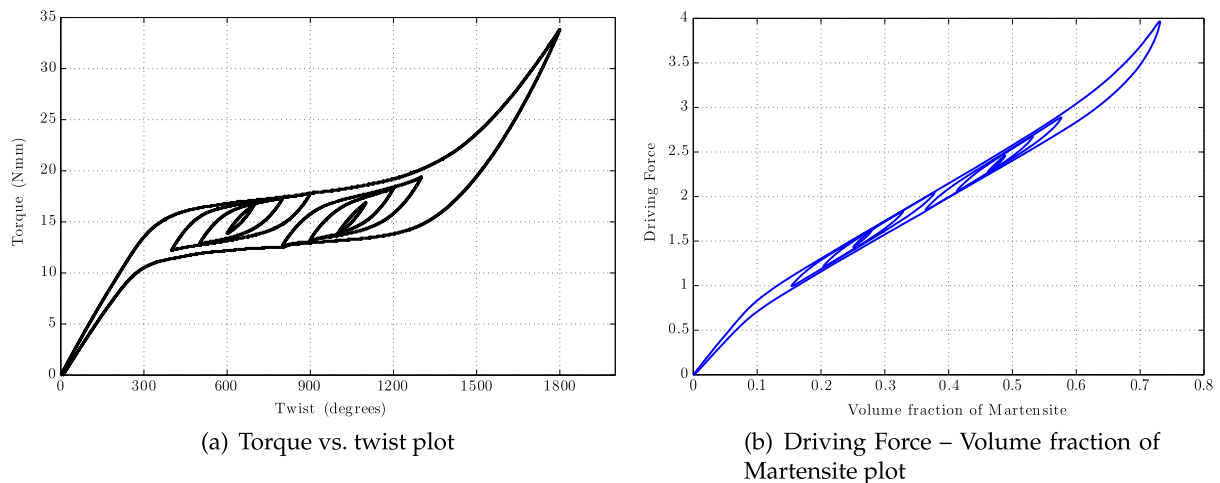


Fig. 12. Torque vs. twist response and its corresponding driving force vs. volume fraction of martensite for wire samples twisted up to 1800° with complex internal loops during loading and unloading cycles.

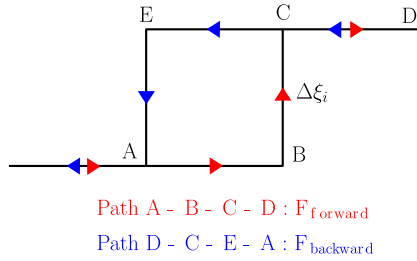


Fig. 13. Basic hysteretic element or hysteron used in the Preisach model. Directions of allowed transformations are represented by the arrows on the hysteron [Rao and Srinivasa, 2013](#).

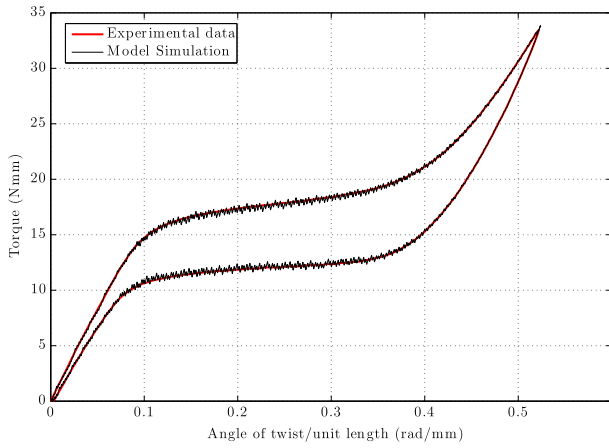


Fig. 14. Data used for model calibration. All predictions discussed in Section 8.1.1 use the hysterons generated for this outer loop response.

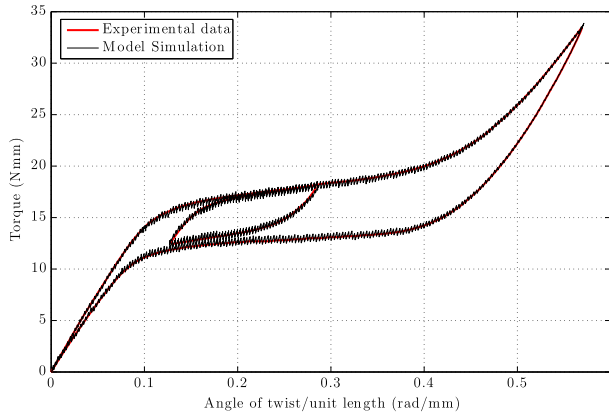


Fig. 15. Simulation for a hysteresis response with one large internal loops during loading cycle. All model predictions discussed in Section 8.2.1 uses the hysterons generated for this experimental data containing the outer loop with one internal loop during the loading cycle.

difference between the two phases. By separating the thermoelastic and the dissipative parts of the entire hysteretic response, one can obtain expressions for the macroscopic thermodynamic driving force for phase transition (refer to Section 4 of [Rao and Srinivasa, 2013](#)).

$$T(\dot{\phi} - \dot{\phi}_e) - \frac{\partial \mathcal{G}}{\partial \xi} \dot{\xi} = P_{\text{inel}} \quad (2)$$

where $\phi_e = \frac{\partial \mathcal{G}}{\partial T}$. With the assumption that $\dot{\phi} - \dot{\phi}_e = \phi_{\text{max}} \dot{\xi}$, where ϕ_{max} is the maximum twist at which the phase transition is complete (generally 6% for NiTi alloys), one can arrive at

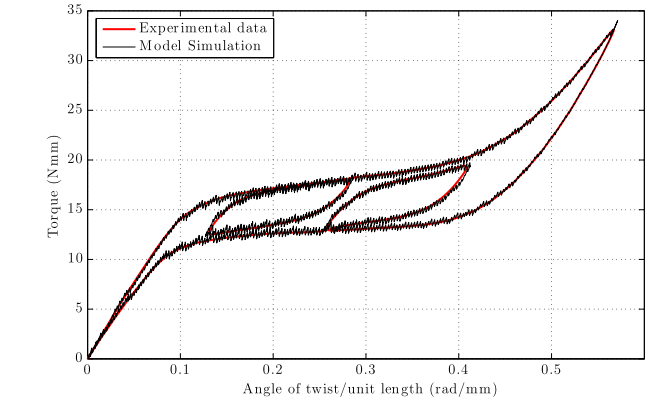
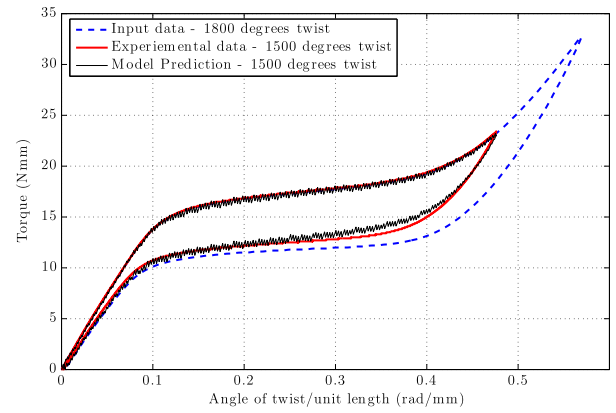
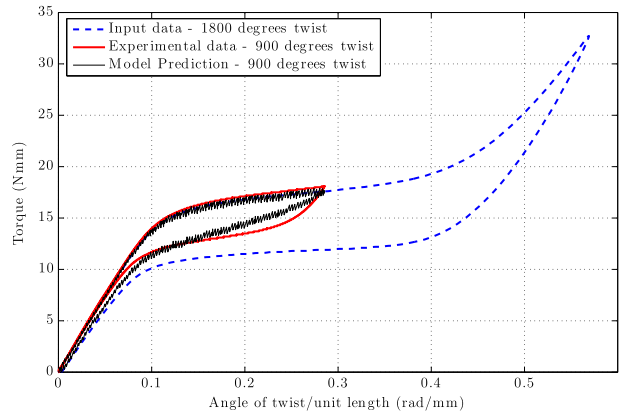


Fig. 16. Simulation for a hysteresis response with an internal loop during the loading and unloading cycle. All model predictions discussed in Section 8.2.2 uses the hysterons generated for this entire outer loop and internal loops during the loading and unloading stages.



(a) Prediction of 1500° twist using 1800 twist data using the input data as shown on figure 14

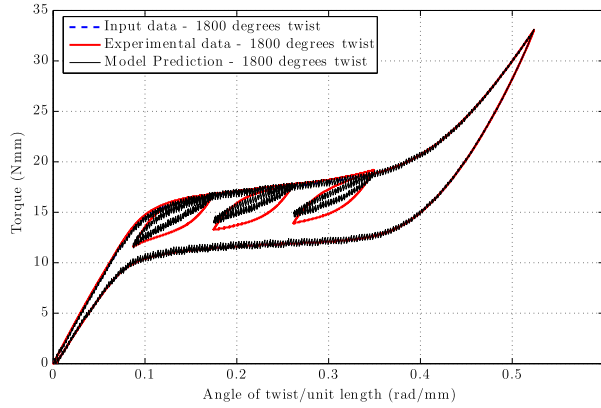


(b) Prediction of 900° twist using 1800 twist data using the input data as shown on figure 14

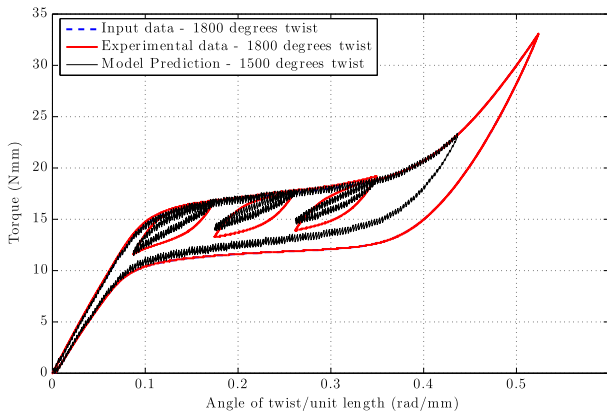
Fig. 17. Figures show the prediction of lower twists 1500° and 900° twist using the hysterons generated with the 1800° data as shown on [Fig. 14](#). The predictions show a close match with the experimental data and the outer loop is well predicted.

$$\left(T\phi_{\text{max}} - \frac{\partial \mathcal{G}}{\partial \xi} \right) \dot{\xi} = P_{\text{inel}} \quad (3)$$

Following [Doraiswamy \(2010\)](#) and [Doraiswamy et al. \(2011\)](#), the driving force for phase transition (\mathcal{F}) is identified as $\left(T\phi_{\text{max}} - \frac{\partial \mathcal{G}}{\partial \xi} \right)$. Thus Eq. (3), can be rewritten as:



(a) Prediction of 1800° twist with three loops during the loading cycle using the input data as shown on figure 14.



(b) Prediction of 1500° maximum twist with three loops during the loading cycle using the input data as shown on figure 14.

Fig. 18. Figures show the prediction of 1800° and 1500° twist using the hysterons generated with the 1800° outer loops data of the simple load and unload case as shown on Fig. 14. Using minimum information, complex responses involving internal loops are predicted and the results show a close fit with outer loops and a good RPM prediction.

$$\mathcal{F}\dot{\xi} = P_{inel} \Rightarrow \mathcal{F} = \left(T\phi_{max} - \frac{\partial \mathcal{G}}{\partial \xi} \right) \quad (4)$$

The rate of mechanical dissipation χ is the net macroscopic inelastic work (P_{inel}) in a closed cycle of state and by the second law of thermodynamics, this must be non-negative i.e.,

$$\chi = \oint P_{inel} dt \geq 0 \quad (5)$$

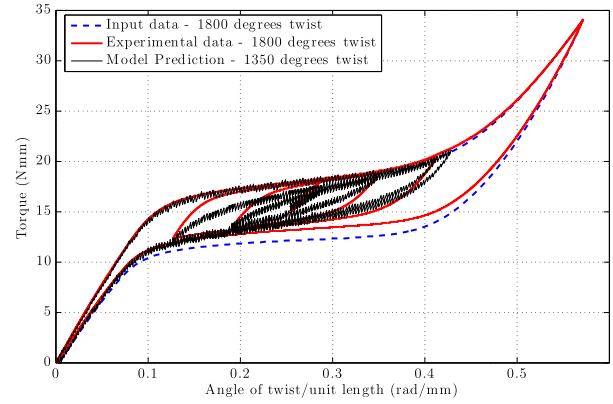
The driving force for phase transformation can be evaluated using Eqs. (1) and (4) and is given by Eq. (6) below.

$$\mathcal{F} = T\phi_{max} + T^2 \left(\frac{1}{2G_M} - \frac{1}{2G_A} \right) - B(2\xi - 1) + b\theta + a \quad (6)$$

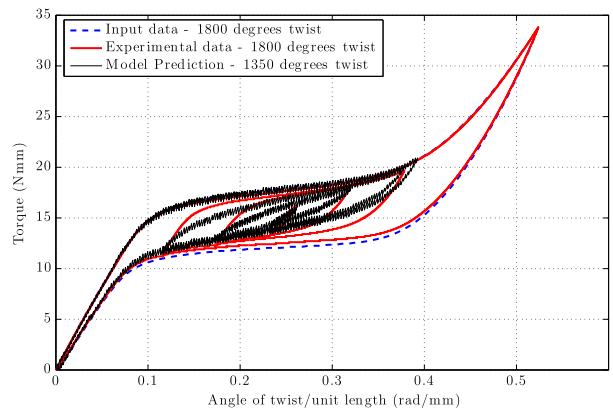
It is clear from the above expression (6) that driving force is a function of torque (T), angle of twist (ϕ), martensitic volume fraction (ξ) and operating temperature (θ).

Further using $\phi_e = \frac{\partial \mathcal{G}}{\partial T}$ and $\phi - \phi_e = \phi_{max}\xi$, an expression for the martensitic volume fraction evolution (ξ) can be obtained as shown in 7 below (refer to Section 4 of Rao and Srinivasa, 2013 for details).

$$\xi = \frac{\phi - \frac{T}{G_A}}{\frac{T}{G_M} - \frac{T}{G_A} + 1} \quad (7)$$



(a) Prediction of 1350° maximum twist with a complex loading loop using the input data as shown on figure 14.



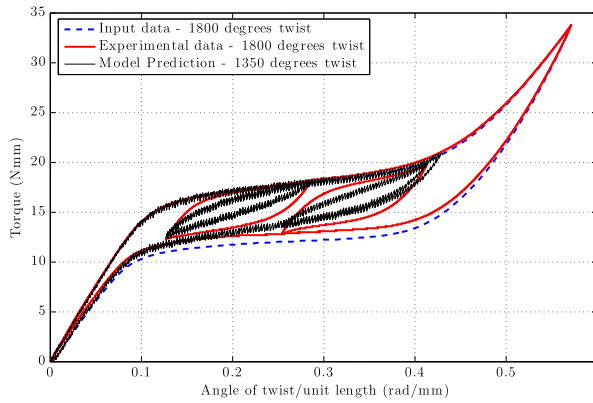
(b) Prediction of 1350° maximum twist with complex unloading loop using the input data as shown on figure 14.

Fig. 19. Figures show the prediction of 1350° maximum twist for complex loop under loading and unloading cases using the hysterons generated with the 1800° outer loops data of the simple load and unload case as shown on Fig. 14. The outer loops are well represented and the complex loops with RPM prediction match well with the experimental data.

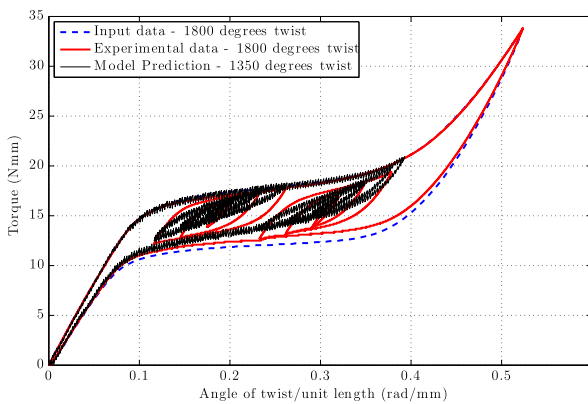
As discussed by Doraiswamy (2010), Doraiswamy et al. (2011) and Rao and Srinivasa (2013), Eqs. (4) and (7) enable us to plot a driving force vs. martensite volume fraction which represents the purely inelastic part of the response. This dissipative part is modeled using a discrete Preisach type approach rather than a purely empirical curve fit to the entire macroscopic measured response. Examples of the driving force vs. volume fraction of martensite obtained with this procedure for the simple loading and unloading case, the three internal loops loading case and complex loops loading and unloading cycles (i.e. experimental test runs discussed in Section 4) are shown in Figs. 10(b), 11(b) and 12(b) respectively.

6. Discrete Preisach model

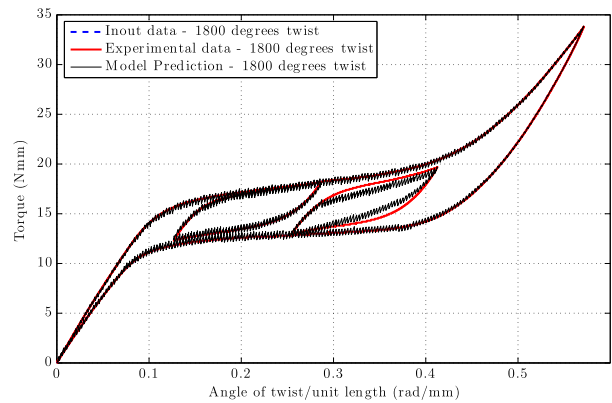
The Preisach model uses a series of hysterons or Preisach elements that behave like a non-ideal switch which turns on and off when the load (or external impetus) increases beyond $F_{forward}$, giving an output $\Delta\xi$ and switches off at $F_{backward}$ as shown on Fig. 13. These types of Preisach models have been employed to capture the entire non-linear hysteretic thermoelastic responses of SMA i.e. either stress strain (see Ortín, 1992) or temperature strain (see Bo and Lagoudas, 1999; Ktena et al., 2001) relationships with Preisach elements. Such purely phenomenological Preisach models



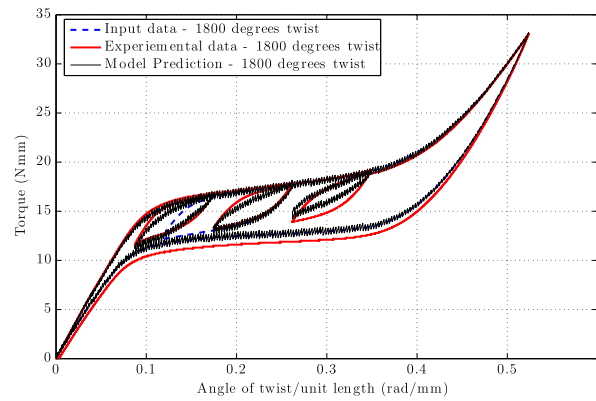
(a) Prediction of 1350° maximum twist with big internal loops during loading and unloading cycles using the input data as shown on figure 14.



(b) Prediction of 1350° maximum twist with complex loading and unloading loops using the input data as shown on figure 14.



(a) Prediction of 1800° twist with internal loops during loading and unloading cycles using the input data as shown on figure 15.



(b) Prediction of 1800° maximum twist with three loops during the loading cycle using the input data as shown on figure 15.

Fig. 20. Figures show the prediction of 1350° maximum twist for two different cases that contain simple and complex loops using the hysterons generated with the outer loops data of the simple load and unload case as shown on Fig. 14. The outer loops are well represented and the complex loops with RPM prediction match well with the experimental data.

have generally no thermodynamic base as they use the entire reversible thermoelastic response. To simulate the response at different temperatures or twists, one would need to use a modified Preisach model.

Following Doraiswamy (2010), Doraiswamy et al. (2011), Rao and Srinivasa (2013), Rao (2013) and Rao and Srinivasa (2014), the driving force–volume fraction of martensite relationships as shown in Figs. 10(b), 11(b), 12(b) for different cases are captured using Preisach elements as described in Appendix B. Such an approach focuses on solely the hysteretic part of the response and not the entire thermoelastic response. With the use of large number of hysterons in series that turn on and off at different driving force values, contribution of each hysteron to volume fractions can be obtained. The three parameters here are $F_{forward}$, $F_{backward}$ and $\Delta\xi$ being the output volume fraction.

6.1. Preisach parameters algorithm

For purposes of completeness, the algorithm used by Doraiswamy (2010) and Doraiswamy et al. (2011) to obtain the Preisach parameters is summarized in Appendix B. Additional details of implementing this discrete Preisach model can be found in Section 5 here (Doraiswamy, 2010; Doraiswamy et al., 2011; Rao and Srinivasa, 2013).

Fig. 21. Figures show the prediction of 1800° twist for two different cases with two and three internal loops using the hysterons generated with the outer loop and one internal loop data as shown on Fig. 15. Using the outer loop and one internal loop information, complex responses involving more internal loops are predicted with the results show a close match to the experimental data.

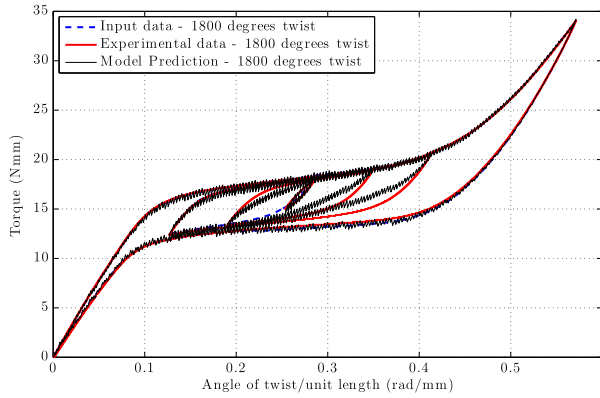
7. Torque vs. angle of twist response – model prediction

The original torque vs. angle of twist is recalculated for both load and displacement controlled tests after the volume fraction ξ for a given driving force \mathcal{F} is estimated using the algorithm described in Appendix B.

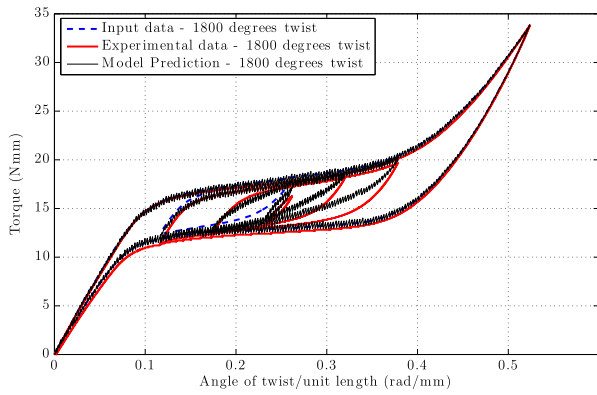
7.1. Load (torque) controlled protocol

If at time t_i , $T(i)$, $\phi(i)$ and $\theta(i)$ are assumed to be known, then by using Eq. (7), $\xi(i)$ can be evaluated. In order to compute these variables at time t_{i+1} , it is assumed that $T(i+1)$ is known. $\mathcal{F}(i+1)$ can now be computed from Eq. (6) for a known $\xi(i)$. Once $\mathcal{F}(i+1)$ is evaluated, the Preisach model is used to predict $\xi(i+1)$. With $\xi(i+1)$ and $T(i+1)$ now known, one can find $\phi_e(i+1)$ and hence $\phi(i+1)$.⁸ In summary, one needs to evaluate the equations below (Doraiswamy, 2010; Doraiswamy et al., 2011; Rao and Srinivasa, 2013; Rao, 2013):

⁸ All the experimental data reported in this work are displacement controlled tests. The model's application for load controlled experiments has been discussed in earlier works. For example, Figs. 8 and 10 in Doraiswamy et al. (2011) illustrates an example for load controlled experiments under tension loading case. An example for SMA spring under load and displacement controlled conditions is also shown in Figs. 7, 8, 11 and 12 in Rao and Srinivasa (2014).



(a) Prediction of 1800° twist with complex loop during the loading cycle using the input data as shown on figure 15.



(b) Prediction of 1800° maximum twist with complex loop during the unloading cycle using the input data as shown on figure 15.

Fig. 22. Figures show the prediction of 1800° twist for two different cases with complex loops during the loading and unloading cycles using the hysteresis generated with the outer loop and one internal loop data as shown on Fig. 15. Using the outer loop and one internal loop information, complex loop responses were predicted and compared against the experimental data.

$$\xi^{(n)} = \sum_{i=0}^n \xi_i^{(n)} \quad (8a)$$

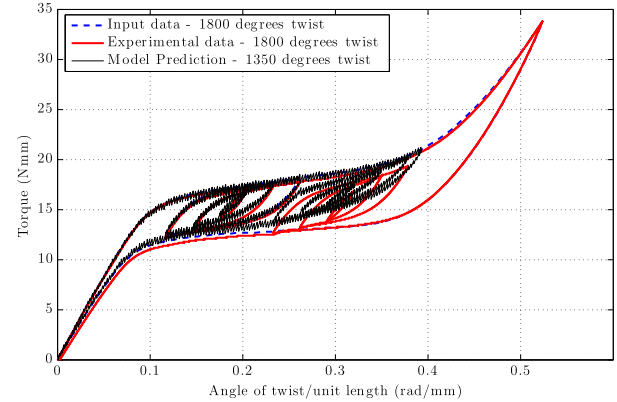
$$\mathcal{F}^{(n+1)} = T^{(n+1)} + \left(T^{(n+1)}\right)^2 \left(\frac{1}{2G_{MI}} - \frac{1}{2G_{AJ}}\right) - B(2\xi^{(n)} - 1) + b\theta + a \quad (8b)$$

$$\phi^{(n+1)} = \frac{\xi^{(n)} T^{n+1}}{G_{MJ}} + \frac{(1 - \xi^{(n)}) T^{n+1}}{G_{AJ}} + \xi^n \quad (8c)$$

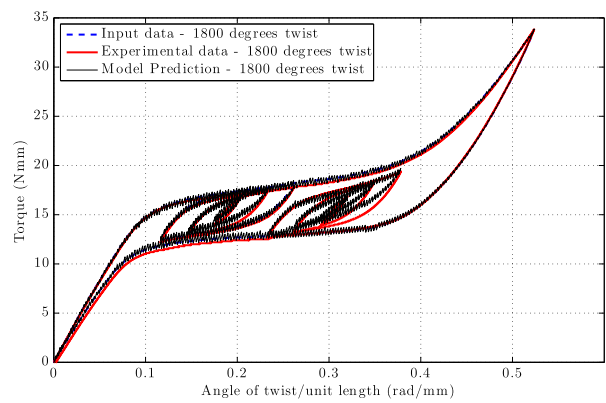
7.2. Displacement (angle of twist) controlled protocol

If at time t_i , $T(i)$, $\phi(i)$ and $\theta(i)$ are known then by using Eq. (7) $\xi(i)$ can be evaluated. Here $\phi(i+1)$ is known and $T(i+1)$ needs to be computed. $\mathcal{F}(i+1)$ is computed using Eq. (6). Now Eq. (7) is used to express T in terms of ϕ and ξ . The Preisach model is used again to find $\xi(i+1)$ from $\mathcal{F}(i+1)$. Once $\xi(i+1)$ and $\phi(i+1)$ are evaluated, using Eq. (7), $T(i+1)$ is evaluated. In summary, one needs to evaluate the equations below (Doraiswamy, 2010; Doraiswamy et al., 2011; Rao and Srinivasa, 2013; Rao, 2013):

$$\xi^{(n)} = \sum_{i=0}^n \xi_i^{(n)} \quad (9a)$$



(a) Prediction of 1350° twist with complex loops during loading and unloading cycles using the input data as shown on figure 15.



(b) Prediction of 1800° twist with complex loops during loading and unloading cycles using the input data as shown on figure 15.

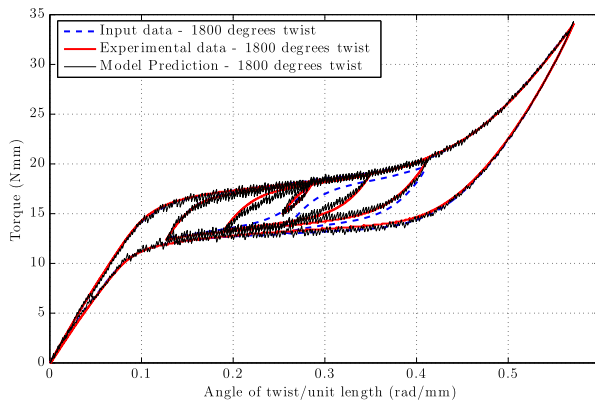
Fig. 23. Figures show the prediction of two cases with maximum twists of 1350° and 1800° using the hysteresis generated with the outer loop and one internal loop data as shown on Fig. 15. Using the outer loop and one internal loop information, complex loops under loading and unloading legs of the response were predicted and compared against the experimental data.

$$T^{(n+1)} = \frac{\phi^{(n+1)} - \xi^{(n)}}{\xi^{(n)} \left(\frac{1}{G_{MJ}} - \frac{1}{G_{AJ}}\right) + \frac{1}{G_{AJ}}} \quad (9b)$$

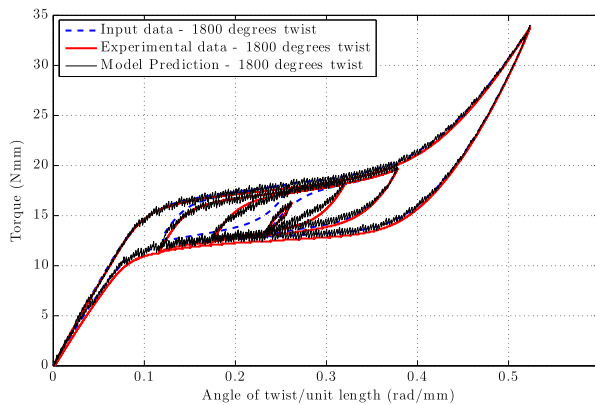
$$\mathcal{F}^{(n+1)} = T^{(n+1)} + \left(T^{(n+1)}\right)^2 \left(\frac{1}{2G_{MJ}} - \frac{1}{2G_{AJ}}\right) - B(2\xi^{(n)} - 1) + b\theta + a \quad (9c)$$

8. Model simulations and predictions

The capability to model internal loops from measurements of quantities from the outer loop is not a trivial task and as alluded to in the abstract none of the models/experiments reported in the literature capture internal loops. As with any model discussed in literature intended to capture the macroscopic responses of SMA components under different loading conditions, the outer loop information is used for model calibration except for those using Ab initio calculations (see Tobushi and Tanaka, 1991; Mirzaeifar et al., 2011, 2010; Chapman et al., 2011; Aguiar et al., 2010; Rao and Srinivasa, 2013; Khan and Srinivasan, 2011; Spinella and Dragoni, 2010; An et al., 2012, etc. for many such examples under torsional loading cases). The approach illustrated below is to demonstrate that it is possible to get progressively increasing fidelity

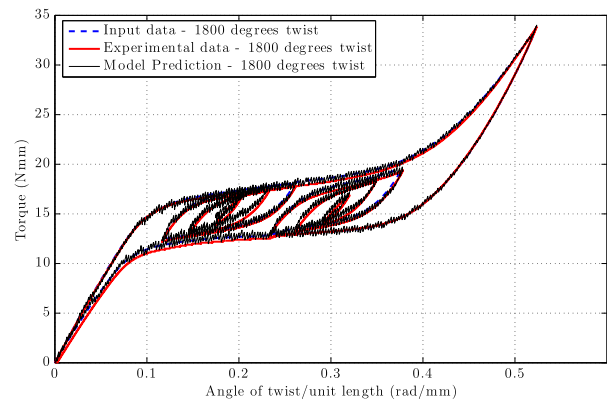


(a) Prediction of 1800° twist with complex loop during the loading cycle using the input data as shown on figure 16

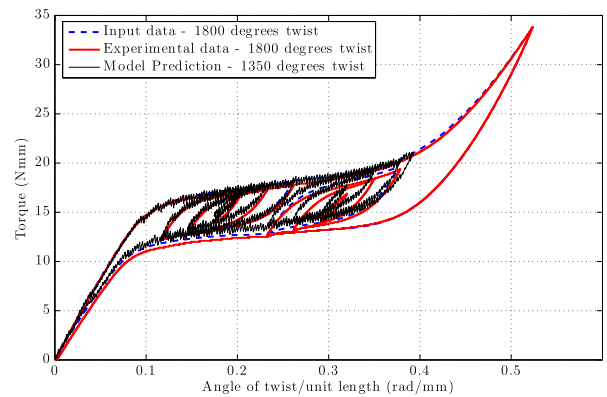


(b) Prediction of 1800° twist with complex loop during the unloading cycle using the input data as shown on figure 16

Fig. 24. Figures show the prediction of complex loops for loading and unloading cases with 1800 maximum twist using the hysterons generated with the outer loop and internal loop during loading and unloading stages as shown with full data simulation discussed on Fig. 16.



(a) Prediction of 1800° twist using the input data as shown on figure 16



(b) Prediction of 1350° twist using the input data as shown on figure 16

Fig. 25. Figures show the prediction of complex internal loops under loading and unloading stages for two cases with 1800° and 1350° maximum twist using the hysterons generated with the outer loop and internal loops during the loading and unloading stages as shown with full data simulation discussed earlier on Fig. 16. The predictions are a close match to the experimental data when compared to earlier predictions as more information that included one big internal loop during loading and unloading stages along with outer loop was used for model predictions.

with increasing data used for model calibration.⁹ Since this is a structural model akin to beam theory, extrapolations are possible for similar geometries/topology. For example, predicting torsional responses of different wire diameters is possible as shown in Fig. 12 (Rao and Srinivasa, 2013) for such an illustration.

8.1. Simulations and predictions using just the outer loop response

Fig. 14 shows a simulation that uses the entire experimental data (outer loop) for model calibration. The Preisach parameters for a given driving force–volume fraction are automatically assigned (as discussed in Appendix B) and the simulation data agrees very well with the experimental data. Results show that the use of a discrete Preisach model results in a jagged response. The model is preferably calibrated at the maximum angle of twist and then used to predict responses at lower twists. For the simulations discussed in this work, a total of 20,100 hysterons were used or equivalently, a Preisach triangle with a side of 200.

⁹ ASTM standard (2007) for the tension loading case defines the two moduli E_A , E_M and the plateau stress (upper and lower) using the outer loop response. Simulations using just the ASTM standard data and the results have been reported elsewhere (see Fig. 8 in Doraiswamy et al., 2011 for an illustration).

8.1.1. Predictions using outer loop information as input data

The model can also be used to predict responses at different degrees of twist. Figs. 17–20 show some examples of model predictions of complex internal loops using just the outer loop response as shown in Fig. 14. The predictions closely mimics the outer loop responses in addition to capturing the simple and complex internal loops (including RPM aspects) especially during the loading stage with reasonable fidelity. These predictions highlight an interesting feature of the thermodynamic Preisach model that it has some predictive capability and is not merely interpolative. One can predict complex inner loops (partially transformed cases) with reasonable fidelity by just using the outer loop data alone with no additional requirements (i.e internal loop information).

8.2. Simulations and predictions using the outer loop and some additional internal loop information

If one uses the entire outer loop with some added internal loop information, greater fidelity with model predictions is to be expected with such Preisach type models. Figs. 15 and 16 show model simulations for such cases which uses the outer loop and some additional internal loop information. These simulations will demonstrate that the details of complex inner loop structures including RPM aspects can be substantially improved if just one inner loop data along with the outer loop is used for model calibration. In subsequent subsections,

various model predictions that use outer loop data with increasing internal loops information for model calibration are discussed.

8.2.1. Model predictions using the entire outer loop with one internal loop during the loading cycle as input data

Some model predictions that use the entire outer loop with one internal loop during the cycle as shown in Fig. 15 is employed for predicting more complex responses. This input data uses an additional internal loop information in addition to the outer loop as discussed in the earlier Section 8.1.1. Figs. 21–23 show some model predictions using this input data. The model predictions captured the outer loop responses with internal loops (including RPM aspects) with a closer match to the experimental data as compared to those discussed in Section 8.1.1 that used only the outer loop for model calibration. Thus, the Preisach model is capable of predicting the complete inner response with only outer loop data, although the use of a single inner loop for calibration improves the predictions. The internal loops during the unloading stages of the model predictions did not exactly match the experimental data as the model input data used only the outer loop and loading cycle internal loop data. Hence, the outer loop and loading cycle internal loops were predicted with reasonable fidelity.

8.2.2. Model predictions using the entire outer loop and one internal loop under loading and unloading stage as input data

Figs. 24 and 25 show some model predictions with complex internal loops using the entire outer loop with additional internal loop information during the loading and unloading stages of the response as input data (as shown on Fig. 16). It is clear that these model predictions (Figs. 24 and 25) agree well with the experimental data as compared to similar predictions discussed in Sections 8.1.1 or 8.2.1 as more internal loop information was used for model calibration. This suggests that the choice of input data for model calibration and choice of Preisach triangle (i.e. number of Preisach elements) can result in a more accurate prediction that is tailored to the level of information available (Rao and Srinivasa, 2013, 2014).

9. Conclusions

In this work, SMA wires were tested to understand the torsional response for various loading and unloading scenarios that can result in simple and complex internal loops under partially and fully transformed cases. Important highlights were:

- The wire response showed excellent return point memory (RPM) for the different internal loops cases investigated.
- Experimental data obtained indicated that the results were repeatable as shown in Fig. 4.
- The samples tested exhibited the formation of stress induced martensite (SIM) with complete recovery upon unloading, an indication of near perfect superelastic/pseudoelastic response.

A thermodynamically consistent Preisach model was used to model complex responses with comparisons against the experimental data.

- The core idea was in separating the thermoelastic and dissipative part of the entire response using thermodynamic principles and a two species Gibbs potential that uses torque and twist information as inputs directly. A discrete Preisach model was later used to capture the dissipative part of the response.
- The model is capable of predicting the complete inner response including RPM aspects with only the outer loop data used for model calibration, although the addition of a single inner loop information for model calibration greatly improved the predictions.

- Predictions are tailored to the level of information available depending on the choice of input data for model calibration. An approximate response prediction could be beneficial for design purposes but a more precise prediction is essential from the control systems standpoint.

Acknowledgments

We acknowledge the support of the National Science Foundation CMMI Grant 1000790 in carrying out this work. We also acknowledge Texas A&M University at Qatar for their support for the visits of Dr. Arun Srinivasa and Dr. Ashwin Rao to Doha, Qatar. We thank Dr. S. Doraiswamy for the Matlab implementation of the Preisach model. Useful discussions with Dr. Vidyashankar Buravalla from GE Global Research is also appreciated.

Appendix A. Discussion on the combined loading case (effect of axial loading along with torsional loads)

Experimental results reported in the literature have shown that normal stresses (i.e. under significantly high axial loads that can nucleate martensite variants) along with the torsional loads can significantly affect the overall combined loading response of SMA component. The effects of combined loading effects under different extents of tension and torsional loads (order matters) for understanding simple outer loop responses have been investigated (Andani et al., 2013a; Grabe and Bruhns, 2008; Han et al., 2005; Lim and McDowell, 1999; McNaney et al., 2003; Sun and Li, 2002). McNaney et al. (2003) have reported experimental data on combined loading cases where the torsional response is significantly affected with tensile strains exceeding 2%. In classical Ni–Ti material system, this is equivalent to stress levels which can nucleate martensite variants at these strains levels i.e. the UPS according to ASTM standard (2007). In a combined loading case, the history of prior deformation (i.e. tension followed by torsion or vice versa) plays an important role in determining the overall hysteretic response. This is due to the fact that the nucleation of different sets of martensite variants (which are energetically preferred) influences the material response depending on the history and extent of loading form McNaney et al., 2003. Further, as observed in Figs. 11, 12 and 14 of McNaney et al., 2003, the overall hysteretic response due to nucleation of multiple martensite variants is significantly affected with “distinct changes” depending on when the tension and/or torsion strains are varied. This is contrary to the unique flat plateau regions observed in classic superelastic responses under tension or torsion loading conditions standalone.

In the experimental data discussed in Section 4, no such “distinct features” as seen in combined loading cases (i.e. McNaney et al., 2003) were observed in all the experimental data reported here. This further validates the fact that the experiments discussed in this work were for pure torsion case. The cause of the distinct features in combined loading cases along with a microscopic understanding of the martensite variants (their nucleation) and their influence on the overall material response is still not well understood and needs more attention.

In many applications, SMA components like torque tubes and SMA springs are used under torsion loading conditions with minimal axial loads. The models available in the literature that consider torque–twist characteristics (or shear stress–shear strain responses for elastoplasticity type models) for such SMA components have shown good agreement with experimental data without accounting for any axial load effects (see Tobushi and Tanaka, 1991; Mirzaeifar et al., 2011; Mirzaeifar et al., 2010; Chapman et al., 2011; Aguiar et al., 2010; Rao and Srinivasa,

2013; Khan and Srinivasan, 2011; Spinella and Dragoni, 2010; An et al., 2012 for many such examples).

With regard to the importance of axial loading, from a modeling perspective, it is important to consider the case of no axial loading first to see the effect of axial load. This work is intended to establish this baseline, including effects of internal loops and the RPM aspects.

One of the big challenges for combined loading cases is the question of what effective load should be used. A von Mises type approach which is based on plasticity of steel is quite widely used to capture combined loading effects. It is unclear that such a yield criterion would even be reasonable for SMAs given that it not suitable even for Aluminum (Rao and Srinivasa, 2013, 2014). Indeed, the work of Andani et al. (2013b) and Andani and Elahinia (2014) demonstrate that the von Mises type criteria are unsuitable and develop criteria that show much better agreement with experiments on outer loops. In addition, SMA wires are drawn and show significant texture and strong anisotropy which adds to the complexity. Hence, the attention in this work is restricted to a pure torsion case.

Improved understanding of phase transformations under combined loading cases and more experimental data to capture the complex hysteretic responses under fully and partially transformed cases (internal loops and RPM aspects) is required.

Appendix B. Preisach algorithm

Following Doraiswamy and co-workers (Doraiswamy et al., 2011; Doraiswamy, 2010; Rao and Srinivasa, 2013, 2014; Rao, 2013), the algorithm for obtaining the Preisach parameters is briefly summarized below. The algorithm allows determination of the contribution of each hysteron is accumulated to get the total volume fraction of martensite for a given driving force.

The state S_i of the i 'th hysteron can take on one of two values: 0 or $\Delta\zeta^i$ where $\Delta\zeta^i$ is the volume fraction of martensite contributed by the i 'th hysteron. At any stage, the extent of transformation, i.e., the volume fraction of martensite evolved, is given by:

$$\zeta = \sum_{i=1}^n S_i \quad (\text{B.1})$$

The state $S_i^{(n)}$ at time t_n is known and hence the state at t_{n+1} is given by:

$$\text{if } S_i^{(n)} = 0 \quad \& \quad \mathcal{F}^{(n+1)} > F_{forward}^i \quad (\text{B.2})$$

$$\text{then } S_i^{(n+1)} = \Delta\zeta_i \quad (\text{B.3})$$

$$\text{if } S_i^{(n)} = \Delta\zeta_i \quad \& \quad \mathcal{F}^{(n+1)} < F_{backward}^i \quad (\text{B.4})$$

$$\text{then } S_i^{(n+1)} = 0 \quad (\text{B.5})$$

$$\text{else } S_i^{(n+1)} = S_i^{(n)} \quad (\text{B.6})$$

At the end of this time step, the $\zeta^{(n+1)}$ is then (as in (B.1)),

$$\zeta^{(n+1)} = \sum_{i=1}^n S_i^{(n+1)} \quad (\text{B.7})$$

Thus, at the end of the time step t_{n+1} , $\zeta^{(n+1)}$ is known, given $\mathcal{F}^{(n+1)}$ and $S_i^{(n)}$ for all the hysterons.

For each hysteron, inelastic power δP_{inel}^i is given by,

$$\delta P_{inel}^i = F \delta\zeta = (F - F_{mean}) \delta\zeta + F_{mean} \delta\zeta \quad (\text{B.8})$$

where $\delta\zeta$ is

$$(\Delta\zeta_i) \text{ if } F > F_{forward}^i \quad \text{or} \quad (-\Delta\zeta_i) \text{ if } F < F_{backward}^i$$

Therefore, the first term in Eq. (B.8) is always positive and the second term is positive or negative depending on $\delta\zeta$. The dissipation in a closed cycle of state (i.e sum of δP_{inel}^i over all hysterons)

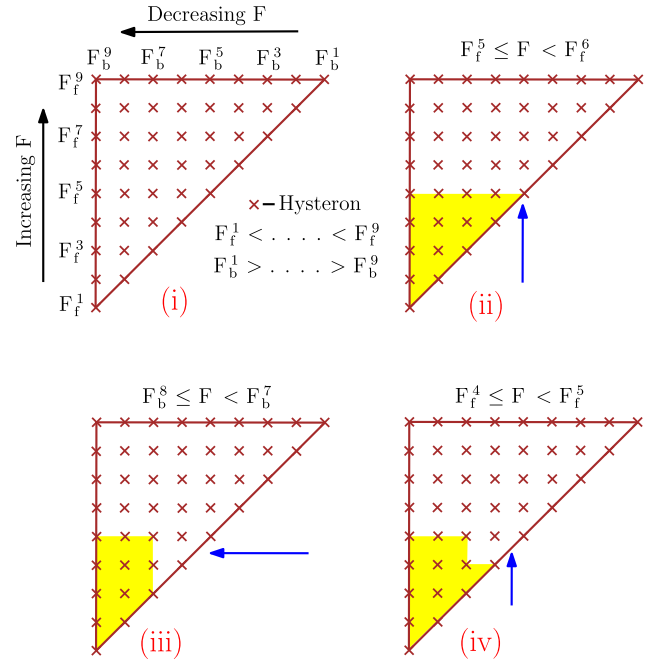


Fig. B.26. (i): Preisach triangle – A systematic way for assigning switch on and switch off of the hysterons. The directions of loading (forward) and unloading (backward) sweeps are marked on the figure. Sub figures (ii)–(iv) shows an example for sequencing of states in the Preisach triangle. The colored section shows the hysterons that are switched on with the corresponding driving force enforcing the state (Doraiswamy, 2010; Doraiswamy et al., 2011; Rao and Srinivasa, 2013, 2014; Rao, 2013).

will always be positive as the first term will be positive whereas the sum of second term will be zero.

Using the above algorithm, the three parameters $F_{forward}^i$, $F_{backward}^i$ and $\Delta\zeta^i$ are computed for each hysteron and the driving forces ($F_{forward}^i$, $F_{backward}^i$) assigned in a systematic way using a Preisach triangle as discussed in the following Appendix B.1. This greatly simplifies the computation of $\Delta\zeta^i$ for each of the hysterons.

B.1. Preisach triangle

The Preisach triangle is a geometric way of arranging hysterons in a systematic way that allows the hysterons to switch on and off (see chapter 1 Mayergoyz, 2003). As shown on Fig. B.26, hysterons are assigned $F_{forward}$ and $F_{backward}$ in a way such that the hysterons on any particular row have the same $F_{forward}$ and the hysterons on any column have the same $F_{backward}$ in the triangle (Doraiswamy, 2010; Doraiswamy et al., 2011; Rao and Srinivasa, 2013). Further, the hysterons with the lowest $F_{forward}$ are positioned at the bottom row of the triangle, and the forward threshold value increases up along the rows. Similarly, the hysterons with the lowest $F_{backward}$ are positioned at the left end of the triangle, and the backward threshold values increase from left to right (Doraiswamy, 2010; Doraiswamy et al., 2011; Rao and Srinivasa, 2013). A few examples of hysteron assignments for different driving force levels are discussed on Fig. B.26.

Once the $F_{forward}$ and $F_{backward}$ values are assigned, one has to determine the corresponding “output”, $\Delta\zeta$ for each hysteron. The number of hysterons in a triangle of side n is $\frac{n(n+1)}{2}$. In order to evaluate $\Delta\zeta$ for each hysteron, a system of equations are setup where each equation corresponds to the sum of the outputs of all those hysterons that are switched on. These are now equated to the volume fraction, ζ from the data (Figs. 10(b), 11(b) and 12(b)) corresponding to the driving force level. Since there are $\frac{n(n+1)}{2}$

hysteron, and only $k\left(\frac{n(n+1)}{2}\right)$ data points (depending on the experimental data), a least squares fit with the non-negativity constraint for the outputs of the hysteron is computed using “CVX”, a MATLAB® package developed for solving convex problems including such least square problems (Doraiswamy, 2010; Doraiswamy et al., 2011; Grant and Boyd, 2008; Grant et al., 2008; Rao and Srinivasa, 2013, 2014).

Appendix C. Supplementary data

Supplementary data associated with this article can be found, in the online version, at <http://dx.doi.org/10.1016/j.ijsolstr.2014.09.002>.

References

- Aguilar, R., Savi, M., Pacheco, P., 2010. Experimental and numerical investigations of shape memory alloy helical springs. *Smart Mater. Struct.* 19, 025008.
- Andani, M.T., Elahinia, M., 2014. A rate dependent tension–torsion constitutive model for superelastic nitinol under non-proportional loading: a departure from von Mises equivalency. *Smart Mater. Struct.* 23, 015012.
- Andani, M.T., Alipour, A., Elahinia, M., 2013a. Coupled rate-dependent superelastic behavior of shape memory alloy bars induced by combined axial–torsional loading: a semi-analytic modeling. *J. Intell. Mater. Syst. Struct.* 24 (16), 1995–2007.
- Andani, M.T., Alipour, A., Eshghinejad, A., Elahinia, M., 2013b. Modifying the torque–angle behavior of rotary shape memory alloy actuators through axial loading: a semi-analytical study of combined tension–torsion behavior. *J. Intell. Mater. Syst. Struct.* 24, 1524–1535.
- An, S.M., Ryu, J., Cho, M., Cho, K.J., 2012. Engineering design framework for a shape memory alloy coil spring actuator using a static two-state model. *Smart Mater. Struct.* 21, 055009.
- 2007e2, F., 2007. ASTM standard test method for tension testing of nickel–titanium superelastic materials. ASTM International, West Conshohocken, PA.
- Attanasi, G., Auricchio, F., Urbano, M., 2011. Theoretical and experimental investigation on SMA superelastic springs. *J. Mater. Eng. Perform.* 20, 706–711.
- Barwart, O., 1996. The effect of temperature change on the load value of Japanese NiTi coil springs in the superelastic range. *Am. J. Orthod. Dentofacial Orthop.* 110, 553–558.
- Bo, Z., Lagoudas, D., 1999. Thermomechanical modeling of polycrystalline SMAS under cyclic loading. Part IV: Modeling of minor hysteresis loops. *Int. J. Eng. Sci.* 37, 1205–1249.
- Bogue, R., 2009. Shape-memory materials: a review of technology and applications. *Assembly Autom.* 29, 214–219.
- Chapman, C., Eshghinejad, A., Elahinia, M., 2011. Torsional behavior of NiTi wires and tubes: modeling and experimentation. *J. Intell. Mater. Syst. Struct.* 22, 1239–1248.
- DesRoches, R., Smith, B., 2004. Shape memory alloys in seismic resistant design and retrofit: a critical review of their potential and limitations. *J. Earthquake Eng.* 8, 415–429.
- DesRoches, R., McCormick, J., Delemont, M., 2003. Cyclic properties of superelastic shape memory alloy wires and bars. *J. Struct. Eng.* 130, 38–46.
- Doaré, O., Sbarra, A., Touzé, C., Moussa, M., Mounni, Z., 2012. Experimental analysis of the quasi-static and dynamic torsional behaviour of shape memory alloys. *Int. J. Solids Struct.* 49, 32–42.
- Dolce, M., Cardone, D., 2001a. Mechanical behaviour of shape memory alloys for seismic applications. 1. Martensite and austenite NiTi bars subjected to torsion. *Int. J. Mech. Sci.* 43, 2631–2656.
- Dolce, M., Cardone, D., 2001b. Mechanical behaviour of shape memory alloys for seismic applications. 2. Austenite NiTi wires subjected to tension. *Int. J. Mech. Sci.* 43, 2657–2677.
- Doraiswamy, S., 2010. Discrete Preisach Model for the Superelastic Response of Shape Memory Alloys (Master's thesis). Texas A&M University.
- Doraiswamy, S., Rao, A., Srinivasa, A., 2011. Combining thermodynamic principles with Preisach models for superelastic shape memory alloy wires. *Smart Mater. Struct.* 20, 085032.
- Drake, S., Wayne, D., Powers, J., Asgar, K., 1982. Mechanical properties of orthodontic wires in tension, bending, and torsion. *Am. J. Orthod.* 82, 206–210.
- El Feninat, F., Laroche, G., Fiset, M., Mantovani, D., 2002. Shape memory materials for biomedical applications. *Adv. Eng. Mater.* 4, 91–104.
- Ghosh, P., Rao, A., Srinivasa, A.R., 2013. Design of multi-state and smart-bias components using shape memory alloy and shape memory polymer composites. *Mater. Des.* 44, 164–171.
- Grabe, C., Bruhns, O., 2008. Tension/torsion tests of pseudoelastic, polycrystalline NiTi shape memory alloys under temperature control. *Mater. Sci. Eng.: A* 481, 109–113.
- Grant, M., Boyd, S., 2008. Graph implementations for nonsmooth convex programs. *Recent Adv. Learn. Control*, 95–110.
- Grant, M., Boyd, S., Ye, Y., 2008. Cvx: matlab software for disciplined convex programming. Online access: <http://cvxr.com/cvx/>.
- Han, Y.L., Xing, D.J., Xiao, E.T., Li, A.Q., 2005. NiTi-wire shape memory alloy dampers to simultaneously damp tension, compression, and torsion. *J. Vib. Control* 11, 1067–1084.
- Heintze, O., Seelecke, S., 2008. A coupled thermomechanical model for shape memory alloys from single crystal to polycrystal. *Mater. Sci. Eng.: A* 481, 389–394.
- Huo, Y., Müller, I., 1993. Nonequilibrium thermodynamics of pseudoelasticity. *Continuum Mech. Thermodyn.* 5, 163–204.
- Ikeda, T., Nae, F.A., Naito, H., Matsuzaki, Y., 2004. Constitutive model of shape memory alloys for unidirectional loading considering inner hysteresis loops. *Smart Mater. Struct.* 13, 916.
- Kapila, S., Sachdeva, R., 1989. Mechanical properties and clinical applications of orthodontic wires. *Am. J. Orthod. Dentofacial Orthop.* 96, 100–109.
- Khan, E., Srinivasan, S.M., 2011. A new approach to the design of helical shape memory alloy spring actuators. *Smart Mater. Res.* 2011, 5. <http://dx.doi.org/10.1155/2011/167195>. Article ID: 167195.
- Khandelwal, A., Buravalla, V., 2011. Models for shape memory alloy behavior: an overview of modeling approaches. *Int. J. Struct. Changes Solids* 1, 111–148.
- Ktena, A., Fotiadis, D., Spanos, P., Massalas, C., 2001. A Preisach model identification procedure and simulation of hysteresis in ferromagnets and shape-memory alloys. *Phys. B: Condens. Matter* 306, 84–90.
- Kumar, M.K., Sakthivel, K., Sivakumar, S., Rao, C.L., Srinivasa, A., 2007. Thermomechanical modeling of hysteresis in SMAS using the dissipationless reference response. *Smart Mater. Struct.* 16, S28.
- Lexcellent, C., Tobushi, H., 1995. Internal loops in pseudoelastic behaviour of Ti–Ni shape memory alloys: experiment and modelling. *Meccanica* 30, 459–466.
- Lim, T.J., McDowell, D.L., 1999. Mechanical behavior of an Ni–Ti shape memory alloy under axial–torsional proportional and nonproportional loading. *J. Eng. Mater. Technol.* 121, 9–18.
- Liu, Y., Xie, Z., Van Humbeeck, J., Delaey, L., 1998. Asymmetry of stress–strain curves under tension and compression for NiTi shape memory alloys. *Acta Mater.* 46, 4325–4338.
- Machado, L., Savi, M., 2003. Medical applications of shape memory alloys. *Braz. J. Med. Biol. Res.* 36, 683–691.
- Manhartsberger, C., Seidenbusch, W., 1996. Force delivery of Ni–Ti coil springs. *Am. J. Orthod. Dentofacial Orthop.* 109, 8–21.
- Matsuzaki, Y., Funami, K., Naito, H., 2002. Inner loops of pseudoelastic hysteresis of shape memory alloys: Preisach approach. In: *SPIE's Ninth Annual International Symposium on Smart Structures and Materials*. International Society for Optics and Photonics, pp. 355–364.
- Mayergoyz, I., 2003. *Mathematical Models of Hysteresis and Their Applications*. Elsevier.
- McNaney, J.M., Imbeni, V., Jung, Y., Papadopoulos, P., Ritchie, R., 2003. An experimental study of the superelastic effect in a shape-memory nitinol alloy under biaxial loading. *Mech. Mater.* 35, 969–986.
- Mirzaeifar, R., DesRoches, R., Yavari, A., 2010. Exact solutions for pure torsion of shape memory alloy circular bars. *Mech. Mater.* 42, 797–806.
- Mirzaeifar, R., DesRoches, R., Yavari, A., 2011. A combined analytical, numerical, and experimental study of shape-memory-alloy helical springs. *Int. J. Solids Struct.* 48, 611–624.
- Miura, F., Mogi, M., Ohura, Y., Hamaoka, H., 1986. The super-elastic property of the Japanese NiTi alloy wire for use in orthodontics. *Am. J. Orthod. Dentofacial Orthop.* 90, 1–10.
- Miura, F., Mogi, M., Ohura, Y., Karibe, M., 1988. The super-elastic Japanese NiTi alloy wire for use in orthodontics. Part III. Studies on the Japanese NiTi alloy coil springs. *Am. J. Orthod. Dentofacial Orthop.* 94, 89–96.
- Miyazaki, S., Otsuka, K., 1989. Development of shape memory alloys. *ISIJ Int.* 29, 353–377.
- Müller, I., 2012. Pseudo-elastic hysteresis in shape memory alloys. *Phys. B: Condens. Matter* 407, 1314–1315.
- Müller, I., Seelecke, S., 2001. Thermodynamic aspects of shape memory alloys. *Math. Comput. Modell.* 34, 1307–1355.
- NDC, Nitinol. Website: <http://www.nitinol.com/>.
- Ortín, J., 1992. Preisach modeling of hysteresis for a pseudoelastic Cu–Zn–Al single crystal. *J. Appl. Phys.* 71, 1454–1461.
- Ortín, J., Delaey, L., 2002. Hysteresis in shape-memory alloys. *Int. J. Non-Linear Mech.* 37, 1275–1281.
- Paiva, A., Savi, M., Braga, A., Pacheco, P., 2005. A constitutive model for shape memory alloys considering tensile–compressive asymmetry and plasticity. *Int. J. Solids Struct.* 42, 3439–3457.
- Prahlad, H., Chopra, I., 2007. Modeling and experimental characterization of SMA torsional actuators. *J. Intell. Mater. Syst. Struct.* 18, 29–38.
- Rajagopal, K.R., Srinivasa, A.R., 1999. On the thermomechanics of shape memory wires. *Z. Angew. Math. Phys. (ZAMP)* 50, 459–496.
- Rao, A., 2013. Modeling bending response of shape memory alloy wires/beams under superelastic conditions – a two species thermodynamic Preisach approach. *Int. J. Struct. Changes Solids* 5, 1–26.
- Rao, A., Srinivasa, A., 2013. A two species thermodynamic Preisach model for the torsional response of shape memory alloy wires and springs under superelastic conditions. *Int. J. Solids Struct.* 50, 887–898.
- Rao, A., Srinivasa, A.R., 2014. A three-species model for simulating torsional response of shape memory alloy components using thermodynamic principles and discrete Preisach models. *Math. Mech. Solids*. SAGE Publications, pp. 1081286514545917.
- Saadat, S., Salichs, J., Noori, M., Hou, Z., Davoodi, H., Bar-On, I., Suzuki, Y., Masuda, A., 2002. An overview of vibration and seismic applications of NiTi shape memory alloy. *Smart Mater. Struct.* 11, 218.

- Savi, M., Paiva, A., 2005. Describing internal subloops due to incomplete phase transformations in shape memory alloys. *Arch. Appl. Mech.* 74, 637–647.
- Sittner, P., Hara, Y., Tokuda, M., 1995. Experimental study on the thermoelastic martensitic transformation in shape memory alloy polycrystal induced by combined external forces. *Metall. Mater. Trans. A* 26, 2923–2935.
- Sittner, P., Stalmans, R., Tokuda, M., 2000. An algorithm for prediction of the hysteretic responses of shape memory alloys. *Smart Mater. Struct.* 9, 452.
- Parts, S., Superelastic nitinol wire (part number: Nw-032-12-10). Website: <<http://www.amazon.com/>>.
- Song, G., Ma, N., Li, H., 2006. Applications of shape memory alloys in civil structures. *Eng. Struct.* 28, 1266–1274.
- Speicher, M., Hodgson, D., DesRoches, R., Leon, R., 2009. Shape memory alloy tension/compression device for seismic retrofit of buildings. *J. Mater. Eng. Perform.* 18, 746–753.
- Spinella, I., Dragoni, E., 2010. Analysis and design of hollow helical springs for shape memory actuators. *J. Intell. Mater. Syst. Struct.* 21, 185–199.
- Spinella, I., Dragoni, E., Stortiero, F., 2010. Modeling, prototyping, and testing of helical shape memory compression springs with hollow cross section. *J. Mech. Des.* 132, 061008.
- Sun, Q.P., Li, Z.Q., 2002. Phase transformation in superelastic NiTi polycrystalline micro-tubes under tension and torsion – from localization to homogeneous deformation. *Int. J. Solids Struct.* 39, 3797–3809.
- Tanaka, K., Nishimura, F., Tobushi, H., 1994. Phenomenological analysis on subloops in shape memory alloys due to incomplete transformations. *J. Intell. Mater. Syst. Struct.* 5, 487–493.
- Tobushi, H., Tanaka, K., 1991. Deformation of a shape memory alloy helical spring (analysis based on stress-strain-temperature relation). *JSME Int. J. Ser. 1. Solid Mech. Strength Mater.* 34, 83–89.
- Williams, K., Chiu, G., Bernhard, R., 2002. Adaptive-passive absorbers using shape-memory alloys. *J. Sound Vib.* 249, 835–848.
- Wilson, J., Wesolowsky, M., 2005. Shape memory alloys for seismic response modification: a state-of-the-art review. *Earthquake Spectra* 21, 569.